



HAL
open science

Inhibitory control of synaptic signals preceding locomotion in mouse frontal cortex

Chun-Lei Zhang, Fani Koukouli, Manuela Allegra, Cantin Ortiz, Hsin-Lun Kao, Uwe Maskos, Jean-Pierre Changeux, Christoph Schmidt-Hieber

► **To cite this version:**

Chun-Lei Zhang, Fani Koukouli, Manuela Allegra, Cantin Ortiz, Hsin-Lun Kao, et al.. Inhibitory control of synaptic signals preceding locomotion in mouse frontal cortex. *Cell Reports*, 2021, 37 (8), pp.110035. 10.1016/j.celrep.2021.110035 . pasteur-03452588v1

HAL Id: pasteur-03452588

<https://pasteur.hal.science/pasteur-03452588v1>

Submitted on 27 Nov 2021 (v1), last revised 29 Nov 2021 (v2)

HAL is a multi-disciplinary open access archive for the deposit and dissemination of scientific research documents, whether they are published or not. The documents may come from teaching and research institutions in France or abroad, or from public or private research centers.

L'archive ouverte pluridisciplinaire **HAL**, est destinée au dépôt et à la diffusion de documents scientifiques de niveau recherche, publiés ou non, émanant des établissements d'enseignement et de recherche français ou étrangers, des laboratoires publics ou privés.



Distributed under a Creative Commons Attribution 4.0 International License

Inhibitory control of synaptic signals preceding locomotion in mouse frontal cortex

Chun-Lei Zhang^{1,*}, Fani Koukoulis^{2,3,+}, Manuela Allegra^{1,x,+}, Cantin Ortiz^{1,4,+}, Hsin-Lun Kao¹, Uwe Maskos², Jean-Pierre Changeux^{5,6}, Christoph Schmidt-Hieber^{1,*,**}

¹ Institut Pasteur, Université de Paris, Neural Circuits for Spatial Navigation and Memory, F-75015 Paris, France

² Institut Pasteur, Université de Paris, CNRS UMR 3571, Integrative Neurobiology of Cholinergic Systems, F-75015 Paris, France

³ Institut Du Cerveau-Paris Brain Institute-ICM, Sorbonne Université, Inserm U1127, CNRS UMR 7225, F-75013 Paris, France

⁴ Sorbonne Université, Collège Doctoral, F-75005 Paris, France

⁵ Institut Pasteur, Université de Paris, Department of Neuroscience, F-75015 Paris, France

⁶ Collège de France, F-75005 Paris, France

* Correspondence: chunlei.zhang@pasteur.fr or christoph.schmidt-hieber@pasteur.fr

** Lead contact

^x Present address: Neuroscience Institute, National Research Council (IN-CNR), Viale Giuseppe Colombo 3, I-35131 Padua, Italy

⁺ These authors contributed equally to this study

SUMMARY

The frontal cortex is essential for organizing voluntary movement. The secondary motor cortex (MOs) is a frontal subregion thought to integrate internal and external inputs before motor action. However, how excitatory and inhibitory synaptic inputs to MOs neurons are integrated preceding movement remains unclear. Here, we address this question by performing *in vivo* whole-cell recordings from MOs neurons of head-fixed mice moving on a treadmill. We find that principal neurons produce slowly increasing membrane potential and spike ramps preceding spontaneous running. After goal-directed training, ramps show larger amplitudes and accelerated kinetics. Chemogenetic suppression of interneurons combined with modeling suggests that the interplay between parvalbumin-positive (PV+) and somatostatin-positive (SOM+) interneurons, along with principal neuron recurrent connectivity, shape ramping signals. Plasticity of excitatory synapses on SOM+ interneurons can explain the ramp acceleration after training. Altogether, our data reveal that local interneurons differentially control task-dependent ramping signals when MOs neurons integrate inputs preceding movement.

INTRODUCTION

The secondary motor cortex (MOs or M2) is thought to be an essential hub for guiding motor action (Barthas and Kwan, 2017; Erlich et al., 2011; Murakami et al., 2014). It receives inputs from numerous sensory cortical and thalamic sources, and projects along the corticospinal tract to the spinal cord and superior colliculus to drive movement output (Donoghue and Wise, 1982; Gabbott et al., 2005). Network connectivity, inactivation experiments, and population recordings suggest that MOs integrates multi-sensory inputs and organizes motor output during voluntary motion (Barthas and Kwan, 2017; Coen et al., 2021).

What are the neuronal correlates of this integration process? In several neural systems, ramp-like signals have been proposed to represent a typical signature of slow integration processes (Mehta et al., 2002; Schmidt-Hieber and Nolan, 2017; Yartsev et al., 2018). Neurons in several fronto-parietal brain regions of rodents and primates, including MOs, also show gradually increasing ramps of spiking activity that reach a threshold level just before the onset of movement (Chen et al., 2017; Hanes and Schall, 1996; Inagaki et al., 2019; Li et al., 2015; Maimon and Assad, 2006; Quintana and Fuster, 1999; Roitman and Shadlen, 2002; Thura and Cisek, 2014). It can occur concurrently in multiple areas within the fronto-parietal cortices (Erlich et al., 2015; Goard et al., 2016). Interactions between several brain regions, including thalamus and cerebellum, contribute to producing and maintaining this ramping neural activity in frontal cortices (Dacre et al., 2021; Gao et al., 2018; Goldman-Rakic, 1995; Tanaka, 2007).

What is the synaptic basis of these integration processes in frontal cortices preceding motor action? While their circuit mechanisms have been extensively studied by extracellular recordings, it is unclear how excitatory and inhibitory synaptic inputs are integrated by individual neurons preceding motor action (Verduzco-Flores et al., 2009). The frontal cortex is characterized by a layered structure containing numerous types of excitatory and inhibitory neurons (DeFelipe and Fariñas, 1992; Kawaguchi and Kubota, 1997). Parvalbumin-positive (PV+) and somatostatin-positive (SOM+) interneurons are two principal subtypes of cortical GABAergic neurons that differ in morphology, physiological properties and targeting of principal neurons (Hangya et al., 2014; Hu et al., 2014; Rudy et al., 2011). Recent intracellular recordings have provided evidence that the interplay between inhibition from these interneurons, excitatory synaptic inputs, and intrinsic membrane properties governs the subthreshold membrane potential dynamics during different locomotor states in several neocortical regions (Gentet et al., 2010; Polack et al., 2013; Schneider et al., 2014). These findings point towards a critical role for synaptic integration of excitatory and inhibitory inputs in shaping neuronal signals preceding motor action in the frontal cortex.

Here we sought to identify how synaptic inputs are integrated during pre-movement neuronal activity by performing *in vivo* whole-cell patch-clamp recordings from MOs principal neurons in awake mice during resting and running on a treadmill. We find that MOs neurons exhibit slowly depolarizing membrane potential ramps (~10 s) preceding the onset of spontaneous movement in both superficial and deep neurons. In spiking neurons, membrane potential ramps are accompanied by slow firing rate ramps with similar dynamics. In animals trained in a goal-directed go/no-go task in a virtual-reality environment, these membrane potential and spike rate ramps are accelerated preceding movement onset. To assess the role of different interneuron subpopulations involved in pre-movement activity in MOs, we chemogenetically suppressed the activity of local PV+ or SOM+ cells in MOs while recording from principal neurons during spontaneous movement periods, unveiling distinct roles for different subtypes of interneurons in shaping task-dependent membrane potential and firing rate ramps preceding the onset of movement.

RESULTS

To explore neuronal dynamics preceding movement onset across different behavioral tasks, we used a setup adapted for rodent head-fixed navigation. Two groups of mice were subject to different behavioral paradigms: a control group of animals performed self-paced spontaneous movement on a treadmill in a dark environment after a brief habituation period, while another group of animals was trained in a goal-directed behavioral task in a virtual-reality (VR) environment (Figure 1A, see Methods). This latter group of animals learned to stop in a reward zone at the end of a linear VR corridor within ~6 days of training, as quantified for example by increased reward and success rates (Figures 1B-1C). To establish the role of MOs in this goal-directed task, we inactivated MOs by bilateral local infusion of muscimol (Figures 1E-1L, see Methods), and found that muscimol application significantly and reversibly reduced behavioral performance, such as reward and success rates, suggesting a specific role for MOs in the goal-directed behavioral task (Figures 1D-1E and 1G-1H). We further analyzed the motor behavior by comparing the durations and frequencies of running and resting periods. Inactivation of MOs led to longer resting periods, while running periods were reduced in frequency but not in duration (Figures 1I-1L). These results are consistent with the interpretation that MOs controls running initiation during the goal-directed task (Barthas and Kwan, 2017; Coen et al., 2021).

To characterize intrinsic membrane properties of MOs principal neurons, we performed *in vivo* whole-cell patch-clamp recordings from head-fixed mice of the control group during resting states

(Figures 2A-2C). Neurons which met basic recording criteria ($n = 47$, see Methods) were split into superficial (150-420 μm) and deep (430-850 μm) recordings according to their depth in MOs (Carlén, 2017; Franklin and Paxinos, 2019; Lein et al., 2007) (Figures 2B-2D; see Methods). Consistent with previous *in vivo* recordings from other neocortical regions (Zhao et al., 2016), superficial MOs neurons (mean recording depth, $303 \pm 16 \mu\text{m}$; $n = 24$) differed significantly from deep neurons ($547 \pm 24 \mu\text{m}$, $n = 23$) in intrinsic membrane properties, with deep neurons showing more depolarized baseline membrane potentials and higher excitability (Figures 2E-2G, details in Table S1).

Motion dependence of membrane potential and firing in MOs principal neurons

How does goal-directed behavior affect membrane potential and firing rate dynamics during resting and running states? To address this question, we recorded from MOs neurons in both groups of mice during locomotor behavior (Figure 3A). 29 out of the 47 recordings from the control group and all 18 of the recordings from the trained group reached the criteria for further analysis of motion-related membrane potential dynamics and firing patterns (see Methods). During electrophysiological recordings, our analysis of motor behavior revealed that trained animals ran more frequently and at higher running speeds (Figures 3B–3F). During spontaneous movement, we observed two populations of MOs neurons with distinct firing rate patterns during resting and running periods: most principal neurons (20 of 29 neurons, 70%) exhibited higher firing rates during resting periods, while a smaller group of neurons (7 of 29 neurons, 24%) showed higher firing rates during running periods (Figure 3G left: resting $0.50 \pm 0.08 \text{ Hz}$ vs running $0.54 \pm 0.24 \text{ Hz}$, $n = 29$; 2 out of 29 neurons were not firing). Notably, in animals trained in the goal-directed task, we observed an opposite trend: more neurons (9 of 18 neurons, 50%) showed higher firing rates during running periods, while 8 of 18 neurons (44%) showed lower firing rates during running than resting periods (Figure 3G right: resting $1.21 \pm 0.33 \text{ Hz}$ vs running $2.42 \pm 0.80 \text{ Hz}$, $n = 18$; 1 out of 18 neurons was not firing). Detailed analysis of membrane potential dynamics revealed that mean membrane potential was more depolarized during running than resting periods in both groups of animals (Figure 3H). The membrane potential increase between resting and running periods was significantly larger during the goal-directed task (Figure 3I). Across neurons, we did not observe any consistent correlation between membrane potential change and animal speed, indicating that state-dependent membrane potential changes cannot be explained by a simple linear relationship with animal speed (Figure S1).

Several previous studies have revealed that the amplitude of membrane potential fluctuations in neocortical neurons decreases promptly upon changes of behavioral states, reflecting a rapid

transition from a synchronized to a desynchronized cortical state (Bennett et al., 2013; Churchland et al., 2010a; Eggermann et al., 2014; Polack et al., 2013; Poulet and Petersen, 2008; Poulet et al., 2012; Schieman et al., 2015; Schneider et al., 2014; Zagha et al., 2013; Zhou et al., 2014). In agreement with these findings, we found that MOs neurons displayed larger subthreshold membrane potential fluctuations during resting periods compared to running periods in the control group (Figure 3J). This decrease in membrane potential fluctuation amplitude was also observed during goal-directed running, similar to the untrained group of animals (Figures 3E-3F and 3J). These fluctuations contained broadband frequency components without any obvious peak in the spectrum before and during movement (Figure S2). Thus, our data indicate that membrane potential fluctuations in MOs neurons rapidly transition from large to small amplitudes, reflecting a change to a desynchronized low-variability state upon movement onset (Churchland et al., 2010a) (Figures 3E-3F, 3J and S2).

Temporal dynamics of ramping signals preceding the onset of movement

To characterize the membrane potential dynamics underlying pre-movement spiking activity, we analyzed recordings with sufficiently long recording periods before and after onset of movement from neurons spontaneously spiking preceding running periods (Figure 4; $n = 11$ out of 29 recordings matching criteria; see Methods). Changes in subthreshold membrane potential (ΔV_m) and firing rates were aligned to the onset of spontaneous running periods of untrained animals (Figures 4A and 4C). This analysis revealed that during spontaneous movement, subthreshold membrane potential displayed a gradual depolarization (~ 10 s) preceding running onset (Figure 4A, individual examples; Figure 4C, summary data). Simultaneously, firing rates averaged across different animals showed slowly and gradually increasing firing rates preceding onset of movement (Figure 4C). To further probe whether signatures of these depolarizing membrane potential ramps could also be found in firing patterns of larger neuronal populations preceding motor action, we performed extracellular recordings of MOs population activity with Neuropixels probe from one untrained mouse (Figures S3A and S3B). These recordings revealed firing rate ramps in putative principal neurons preceding spontaneous movement with similar temporal dynamics as observed in our whole-cell recordings (Figures S3C and S3D). In particular, a steady increase in pre-motion firing rates could be observed in sparsely firing neurons (Figure S3E) that matched the mean firing rates observed during whole-cell recordings (Figure 4C).

To probe how goal-directed training affects synaptic integration during the transition from resting to running, we also analyzed membrane potential and firing rates preceding movement onset in whole-cell recordings from animals trained in the goal-directed task ($n = 10$ out of 18 recordings

matching criteria; see Methods). Strikingly, after training, membrane potential ramps were accelerated (~6 s) (Figure 4B, individual examples; Figure 4D, summary data). Simultaneously, we observed faster spike ramps with a larger amplitude preceding movement onset in these recordings (Figure 4D). Thus, the dynamics of both sub- and suprathreshold ramping activity appears to depend on the nature of the behavioral task.

Previous work has suggested that MOs integrates multisensory information before motor action (Barthas and Kwan, 2017; Coen et al., 2021). Whisker motion constitutes a readily observable manifestation of sensory integration. We therefore captured whisker movements of animals across several sessions during goal-directed training in the VR environment (Figure S4A). Inspection of the training videos showed that whisker movement preceded running periods in ~50-60% of running periods (Figures S4B-S4C; see Methods). Detailed quantification of these whisker precession times revealed that they depended on the training state of the animal, with longer whisker precession times in untrained compared to trained animals (Figure S4D). Across ~6 days of training sessions, whisker precession times decreased from ~9 s to ~6 s (Figure S4E), comparable to the temporal dynamics of membrane potential and firing rate ramps preceding running onset (Figure 4). To further explore the role of MOs in processing whisker signals, we analyzed whisker movement when MOs was bilaterally inactivated by muscimol application (Figure 1F). Inspection of the training videos revealed that gross whisker movement was intact when MOs was inactivated (Figures S4F-S4H; see also Figures 1E-1L). Thus, while parts of MOs also contribute to controlling whisker movement (Ebbesen et al., 2018), our observations are consistent with the view that the ramps represent integration of multi-sensory information, including from the whiskers, preceding running onset.

Previous studies have revealed differences in neuronal activity between neurons in superficial and deep layers of the frontal motor cortex in a whisker-based motor planning task (Chen et al., 2017; Wagner et al., 2019). As recordings from superficial and deep neurons in our data set showed differences in baseline membrane potential and intrinsic membrane properties (Figures 2E-2G), we analyzed superficial and deep recordings separately (Figures S5-S6). This analysis revealed more pronounced changes in membrane potential and firing rates after behavioral training in deep compared to superficial neurons (Figure S6A-S6C), while pre-movement membrane potential dynamics were comparable across layers (Figure S6D-S6I).

Local inhibitory neurons disinhibit principal neurons and shape membrane potential ramps

Emerging evidence suggests that disinhibition plays a critical role in enhancing neuronal activity during diverse behavioral functions (Letzkus et al., 2015; Wolff et al., 2014). To test the role of disinhibition in shaping the membrane potential dynamics of MOs neurons, we chemogenetically suppressed the activity of local PV+ or SOM+ interneurons in MOs (see Methods) while recording from principal neurons during spontaneous movement periods (Figures 5A-5C). In line with previous reports (Jackson et al., 2018), chemogenetic inactivation of PV+, but not of SOM+ interneurons, resulted in an increase of basal firing rates and membrane potential fluctuations of MOs principal neurons, without affecting the mean membrane potential when animals were resting on the treadmill (Figures 5D-5F). Chemogenetic inactivation of PV+, but not SOM+ interneurons, increased the movement-related firing rates of MOs principal neurons during running periods (Figure 5G). When we inactivated PV+ interneurons, we observed that 9 out of 14 principal neurons (64%) exhibited higher firing rates during running compared to resting periods (6 out of 9 superficial recordings, and 3 out of 5 deep recordings; details in Table S1). During inactivation of SOM+ interneurons, 6 out of 12 principal neurons (50%) exhibited higher firing rates during running periods (6 out of 9 superficial recordings, and 0 out of 3 deep recordings; details in Table S1). However, a larger depolarization of principal neurons during transition between resting and running periods was only observed after inactivation of PV+, but not of SOM+ interneurons (Figures 5H-5I). By contrast, we still observed a decrease of membrane potential fluctuations when either PV+ or SOM+ interneurons were inactivated (Figure 5J). Thus, our results suggest that PV+ and SOM+ interneurons produce differential effects on membrane potential and firing rates of principal neurons during different locomotor states.

We next sought to assess the differential roles of SOM+ and PV+ cells in shaping membrane potential ramp dynamics preceding movement onset. To consistently compare the effects of inactivation of different interneurons with our control data, we focused only on recordings from spontaneously spiking principal neurons with sufficiently long recording durations before and after running periods (Figure 6; $n = 8$ spiking recordings during inactivation of PV+, depth: $338 \pm 48 \mu\text{m}$; $n = 7$ spiking recordings during inactivation of SOM+, depth: $359 \pm 41 \mu\text{m}$; details in Table S1). We observed that during inactivation of PV+ interneurons, both subthreshold membrane potential and firing rate ramps were still preserved, without substantial changes in their duration (~ 10 s) (Figures 6A and 6C). By contrast, membrane potential and firing rate ramps were abolished by inactivation of SOM+ interneurons (Figures 6B and 6D). When we compared membrane potential ramps between inactivation of interneurons and control recordings, we found that inactivation of PV+ cells increased the amplitude of ramps (Figures 6C and S7A), while inactivation of SOM+ interneurons depressed the ramps (Figures 6D and S7B). Notably, before

the onset of movement, we observed a sustained depolarization of membrane potential in MOs principal neurons during inactivation of PV+, but not of SOM+ interneurons, compared to control recordings (Figures S7C-S7D). Thus, our data show that inactivation of PV+ interneurons leads to depolarized, large-amplitude membrane potential ramps during spontaneous running periods, resembling those observed after goal-directed training (Figures 4C-4D, 6C and S7C). Moreover, inactivation of SOM+ cells abolishes slow membrane potential ramps (Figure 6D) without changing the baseline membrane potential (Figure S7D). In addition, extracellular recordings from putative interneurons revealed specific changes in their firing activity both before and after the onset of spontaneous running periods (Figures S3F-S3G). While these recordings do not distinguish between PV+ and SOM+ interneurons, they generally support the view that interneurons play specific roles in shaping ramping signals during the transition between resting and running states.

Concerted action of external inputs and local inhibition drives task-dependent ramping signals

In cortical circuits, PV+ interneurons mainly exert fast and powerful perisomatic inhibition on principal neurons and other PV+ cells, while SOM+ interneurons mainly form inhibitory synapses onto distal dendrites of principal neurons and PV+ cells (Cottam et al., 2013; Hangya et al., 2014; Hu et al., 2014; Pfeffer et al., 2013; Rudy et al., 2011). To obtain a better understanding of the differential role of SOM+ and PV+ interneurons in shaping neuronal dynamics preceding movement onset, we developed a simple model of the local MOs circuit (Figure 7; see details in Table S2). PV+, SOM+ and principal neurons were modeled as rate-based variables. All 3 types of neurons received external thalamocortical input (Ährlund-Richter et al., 2019) that increased in activity in a step-like manner preceding movement onset. The SOM+ cell inhibited both the PV+ interneuron and the principal neuron, whereas the PV+ cell mainly inhibited the principal neuron. The principal neuron excited both interneuron units and itself in a recurrent manner. As has previously been shown (Chaudhuri and Fiete, 2016; Economo et al., 2018; Gao et al., 2018; Li et al., 2016; Murakami et al., 2014), the recurrent connectivity of the principal neuron, in concert with inhibition from PV+ and SOM+ cells, resulted in a conversion of the step-like external input into a slowly increasing and sustained ramp of activity (Figure 7A), which is consistent with our experimental observations (Figures 4 and S6). Inactivation of the SOM+ cell led to disinhibition of the PV+ interneuron and consequently to silencing of the principal neuron, thereby abolishing the ramp (Figure 7B). By contrast, inactivation of the PV+ cell led to disinhibition of the principal neuron, resulting in a ramp with a steeper slope and in increased baseline activity (Figure 7C).

Both of these simulation results were qualitatively consistent with our experimental observations of membrane potential dynamics during inactivation of PV+ or SOM+ interneurons (Figures 6 and S7). Our simulations further revealed that increasing excitatory synaptic weights on the SOM+ cell could accelerate the temporal dynamics and amplitude of the ramping activity by changing the SOM+/PV+ activity balance over time (Figure 7D). These simulations show that the interplay between SOM+ and PV+ interneuron activities can explain their roles in shaping the ramping dynamics in principal neurons, in agreement with our experimental findings (Figures 6 and S7). Moreover, our model reveals that potentiation of excitatory synapses onto SOM+ cells changes the balance between SOM+ and PV+ interneuron activities, leading to decreased PV+ activity preceding movement onset and during running period (Figure 7D). These dynamics can thereby contribute to the acceleration of the ramp that we observe after goal-directed training (Figures 4 and S6).

DISCUSSION

Using *in vivo* whole-cell patch-clamp recordings from principal neurons in the secondary motor cortex, we explore how excitatory and inhibitory synaptic inputs are integrated preceding running onset. We observe that both superficial and deep neurons display different neuronal activity dynamics depending on whether the animal was trained to perform a behavioral task: untrained animals show slow (~10 s) ramps of membrane potential and spike rates preceding spontaneous movement periods, whereas in animals trained to perform a goal-directed task, the dynamics of both membrane potential and spike ramps are faster (~6 s) and larger in amplitude. At the same time, membrane potential fluctuations rapidly decrease in amplitude upon onset of running, independently of the training state of the animal. To understand how these dynamics are generated at the cellular and circuit level, we manipulated the activity of specific interneuron subpopulations using chemogenetic tools. Inactivation of PV+ interneurons disinhibits MOs principal neurons and increases the amplitude of membrane potential ramps, while inactivation of SOM+ cells abolishes membrane potential ramps. However, local inactivation of PV+ or SOM+ interneurons does not affect the running-related decrease in membrane potential fluctuation amplitude. Therefore, our results suggest that the concerted action of external inputs and local inhibition shapes pre-movement ramping signals in MOs.

Circuit mechanisms underlying motion-related transitions in subthreshold membrane potential fluctuations

Several mammalian brain regions transition between synchronized and desynchronized regimes when adapting to changes between different behavioral states or responding to different stimuli (Buzsáki and Draguhn, 2004; Churchland et al., 2010a; Harris and Thiele, 2011; Lee and Dan, 2012). Slow subthreshold fluctuations during synchronized states have previously been observed during resting periods in somatosensory, visual, and auditory cortices of head-restrained mice. When animals start to move or attend to a stimulus, these cortical neurons rapidly transition to a desynchronized low-variability state (Bennett et al., 2013; Churchland et al., 2010a; Eggermann et al., 2014; Polack et al., 2013; Poulet and Petersen, 2008; Poulet et al., 2012; Schieman et al., 2015; Schneider et al., 2014; Zaghera et al., 2013; Zhou et al., 2014). Consistently, we observed that most MOs principal neurons showed large subthreshold fluctuations during resting periods, and transitioned to a low-fluctuation state during running periods (Figures 3J and S6C). Thus, our results suggest that neurons in MOs evolve from a synchronized to a desynchronized state upon running onset.

Which mechanisms can explain membrane potential fluctuation variability? Membrane potential fluctuations are governed by the interplay between intrinsic membrane properties and excitatory and inhibitory synaptic inputs. Excitatory and inhibitory neurons in the barrel cortex have been shown to affect subthreshold fluctuations during quiet wakefulness (Gentet et al., 2010). In our experiments, chemogenetic inactivation of PV+, but not of SOM+ interneurons, results in higher firing rates and increased subthreshold membrane potential fluctuations during resting periods (Figures 5D-5F). Local PV+ cells in the auditory cortex have been suggested to play a role in controlling motion-related membrane potential fluctuation amplitudes (Schneider et al., 2014). However, we observed that chemogenetic suppression of local PV+ interneurons reversed the motion-related firing pattern of principal neurons (Figure 5G), but left the decrease of subthreshold fluctuations upon movement onset unaffected (Figure 5J). Thus, our results support the view that the motion-related decrease in membrane potential fluctuations is driven by a desynchronization of external inputs (Churchland et al., 2010a) rather than by increased activity of local interneurons. What could be the source of these external inputs? It has been suggested that coordinated activity in a multiregional loop spanning cerebellum, thalamus and frontal cortex is required for motor action (Gao et al., 2018; Guo et al., 2014, 2017; Wagner et al., 2019). At the anatomical level, frontal cortex projects to the cerebellum via the basal pontine nucleus, and cerebellum projects back to frontal cortex via the thalamus (Ährlund-Richter et al., 2019; Economo et al., 2018; Gao et al., 2018; Guo et al., 2017; Li et al., 2015). Therefore, thalamic projections to the neocortex play a crucial role in driving cortical sensory processing (Fuster and Alexander, 1971; Lara et al., 2018). How do these thalamo-cortical synapses modulate movement-related membrane potential dynamics? In a goal-directed motor task, silencing thalamic inputs to primary motor cortex blocks characteristic movement-related membrane potential dynamics and movement initiation (Dacre et al., 2021). Similarly, during whisking, membrane potential depolarization and desynchronization of the cortical state are driven by increased thalamic activity (Dacre et al., 2021; Poulet et al., 2012). These previous studies suggest that thalamic inputs may also drive the pre-movement ramping activity that we observe in MOs as part of a feedback loop, and the concerted action of these external inputs with local inhibition shapes the ramping signals in MOs before onset of movement (Figure 7A).

Information flow in the MOs circuit preceding movement

It has been proposed that MOs is important for integration of multisensory inputs before motor action (Barthas and Kwan, 2017; Coen et al., 2021). As previous studies have used extracellular recordings, how synaptic inputs are integrated by MOs neurons preceding onset of movement has not been revealed yet. Our intracellular recordings from silent and firing MOs neurons show that both types of cells integrate synaptic inputs to produce slowly depolarizing membrane potential ramps preceding the onset of movement (Figures 4 and S6). In the neocortex, information from the thalamus and cortical areas is transmitted in a directional manner from superficial to deep layers (Bureau et al., 2006; Lübke and Feldmeyer, 2007; Otsuka and Kawaguchi, 2008). Selective activation of deep layer 5 cells by superficial layer 2/3 neurons may facilitate this directional transfer of information (DeFelipe and Fariñas, 1992; Kampa et al., 2006; Otsuka and Kawaguchi, 2008). Superficial layers are thought to be the principal recipient for sensory information (Mao et al., 2011). By contrast, deep neurons in layer 5 of frontal areas produce movement output signals. For example, deep neurons from the anterior-lateral motor region play a distinct role in initiating ramping activity in preparation of movement (Chen et al., 2017; Guo et al., 2014). These movement signals are then sent along the thalamus and the corticospinal tract to the spinal cord and superior colliculus to drive movement output in coordination with the cerebellum (Donoghue and Wise, 1982; Economo et al., 2018; Gabbott et al., 2005). We find that both superficial and deep MOs neurons display slowly depolarizing membrane potential ramps preceding movement onset by several seconds (Figures S6D-S6I). However, deep neurons are more depolarized and excitable than superficial neurons (Figures 2E-2G), rendering them more sensitive to changes in their inputs. Accordingly, neuronal spiking dynamics are more strongly affected by the training state of the animal in deep cells compared to superficial cells, as we observe a pronounced increase of firing rates only in deep neurons after behavioral tasks (Figure S6A). Together, our results support the view that excitatory synaptic inputs are processed in a feed-forward manner from superficial to deep layers, resulting in task-dependent output from deep cortical neurons that exerts top-down influences in information processing (Gilbert and Sigman, 2007).

Inhibitory role of PV+ interneurons in pre-movement ramping signals

After goal-directed training, MOs neurons were more depolarized before and after onset of movement compared to neurons from spontaneously running animals (Figure S6F and S6I). At the same time, the mean membrane potential during resting periods was not significantly different between the two groups (Figure 3H). How can we explain the sustained seconds-long

depolarization preceding onset of movement? Our chemogenetic experiments indicate that inactivation of PV+, but not of SOM+ interneurons, results in a large and persistent depolarization of principal neurons preceding movement onset and during running (Figure S7C), without changing the mean membrane potential during resting periods (Figure 5E). In addition, we also find that inactivation of PV+ cells substantially increases membrane potential fluctuation amplitudes and firing rates during resting periods (Figure 5D and 5F). Furthermore, inactivation of PV+, but not of SOM+ interneurons, drives membrane potential towards threshold before the onset of running (Figures 5H-5I), resulting in a higher firing rate during the subsequent running periods (Figure 5G). Thus, a reduction of PV+ interneuron activity during running periods in trained animals can explain several key aspects of our data. Studies in other brain regions support our conclusions: in the barrel cortex, the firing of PV+ cells dominates during quiet wakefulness (Gentet et al., 2010). Similarly, in other neocortical regions, a reduction of PV+ IN activity has been shown to affect membrane potential dynamics and neuronal firing during running states (Polack et al., 2013; Schneider et al., 2014). By contrast, inactivation of SOM+ cells leads to more heterogeneous effects on principal neurons: overall, membrane potential and firing rates during movement show less changes than during PV+ interneuron inactivation (Figures 5D-5E and 5G-5I).

Disinhibitory role of SOM+ interneurons in shaping membrane potential ramps

PV+ interneurons densely target the perisomatic domains of principal neurons across cortical areas and layers (Packer and Yuste, 2011). By contrast, SOM+ cells densely target the tuft, apical and basal dendrites of principal neurons in a layer-specific manner (Fino and Yuste, 2011; Wang et al., 2004). Converging evidence suggests that PV+ cells strongly inhibit each other without inhibiting other interneuron subtypes, whereas SOM+ strongly inhibit PV+ interneurons across all layers without inhibiting themselves (Ährlund-Richter et al., 2019; Cottam et al., 2013; Pfeffer et al., 2013). Such a pattern of connectivity might define their distinct roles in shaping neural dynamics in the MOs neuronal network: a general and unimodal inhibitory role for PV+ interneurons, and a specific and cross-modal role in experience-dependent plasticity for SOM+ cells (Figure 7). For example, recent evidence has shown that such SOM+ interneuron-mediated inhibition of PV+ cells may be important to disinhibit MOs principal neurons during encoding of cue associations in an associative fear learning task (Cummings and Clem, 2020), and to synchronize network activity in the prefrontal cortex during fear expression and social discrimination (Courtin et al., 2014; Scheggia et al., 2020). If activation of SOM+ cells was exclusively and unimodally providing dendritic inhibition to principal neurons, their inactivation

should result in depolarization of excitatory neurons. By contrast, we observe that inactivation of SOM+ interneurons abolishes membrane potential ramp without affecting the mean baseline membrane potential (Figures 6D and S7D). We therefore suggest that SOM+ cells disinhibit principal neurons via inhibition of PV+ interneurons, resulting in a slow depolarizing membrane potential ramp preceding the onset of movement (Figure 7). In agreement with our suggestion, other studies have shown that during maintenance of working memory, the activity of PV+ interneurons in medial prefrontal cortex is reduced during delay periods and strongly inhibited during reward-taking periods. By contrast, SOM+ cells show a strong activation during delay periods (Kim et al., 2016a). The role of additional types of interneurons, such as vasoactive intestinal peptide (VIP) expressing cells, shown to act mainly through indirect disinhibition of principal neurons via inhibition of SOM+ and PV+ cells (Koukoulis et al., 2017; Lee et al., 2013; Pi et al., 2013), remains to be explored.

SOM+ plasticity can explain ramp acceleration after learning a goal-directed task

Our experiments and computational modelling suggest that PV+ and SOM+ interneurons also play a key role in producing faster membrane potential ramps with larger amplitudes preceding onset of goal-driven movement (Figure 4D). Inactivation of PV+ interneurons during spontaneous movement results in depolarized membrane potential ramps with larger amplitudes, thereby reproducing some of the features of the ramps after goal-directed training. However, PV+ inactivation fails to reproduce the ramp acceleration that we observe before onset of goal-directed movements (Figures 6C and S7A). To fully capture all dynamics of ramping pre-movement signals after goal-directed training, we therefore suggest that excitatory inputs to SOM+ interneurons undergo task-specific experience-dependent plasticity (Biane et al., 2016). In agreement with this suggestion, other studies have shown that excitatory synaptic inputs targeting prefrontal SOM+ cells are potentiated after cue fear acquisition, thereby boosting their efficacy of disinhibition of principal neurons via potent inhibition of PV+ cells (Cummings and Clem, 2020). A similar mechanism could explain our observations: our modelling suggests that after goal-directed tasks, potentiated activity of SOM+ cells might exert more efficient inhibition of PV+ interneurons just before and during running periods, resulting in faster and larger depolarizing membrane potential ramps (Figure 7D).

Temporal dynamics of membrane potential ramp signals preceding motor action

As neural transmission within isolated neurons and circuits shows intrinsic time constants on the scale of milliseconds, how can ramping activity persist during several seconds preceding

movement onset? Experiments and computational modelling have shown that sustained ramping activity can result from neuronal modules that integrate transient inputs (Murakami et al., 2014). The robustness of the ramping activity to large transient perturbations furthermore suggests that the network dynamics of these integrator modules in the cerebellar-thalamic-frontal network is independent, redundant and coupled through feedback connections during motor preparation (Chaudhuri and Fiete, 2016; Economo et al., 2018; Gao et al., 2018; Inagaki et al., 2019; Li et al., 2016; Murakami et al., 2014). Preparatory ramping signals are thought to be initiated in frontal motor regions, from where they enter the loop and evolve during several seconds preceding motor action (Churchland et al., 2010b; Gao et al., 2018; Li et al., 2015), regardless of how movements are initiated (Lara et al., 2018). Together, these studies propose that multi-circuit mechanisms for maintaining ramping activity underlie the role of motor-associated cortices in the temporal organization of motor behaviors (Svoboda and Li, 2018). Consistently, our computational modelling shows that recurrent connectivity of MOs principal neurons, in concert with inhibition from PV+ and SOM+ interneurons, can convert a step-like external input into a slowly increasing and sustained ramp of activity (Figures 4 and 7).

Recent evidence suggests that MOs acts as a multisensory integration hub for adaptive choice behavior (Barthas and Kwan, 2017). The depolarizing ramp that we observe may represent integration of multisensory information predicted by a recent model of the MOs circuit (Coen et al., 2021). Our whole-cell recordings, which sample from neurons without any bias for their firing rates, reveal that the synaptic integrative processes underlying the depolarizing ramp may occur at a much slower rate than was previously expected, in particular preceding spontaneous running periods. Such slow integration processes may have important implications for the synaptic and circuit basis of decision making.

Limitations of the study

In the present study, we propose a circuit basis for ramping signals preceding movement and hypothesize that they represent integration of external and internal inputs by MOs neurons that control movement onset once a threshold is reached. We do not provide causal evidence for this hypothesis though. Such a demonstration would require specifically blocking ramping signals during movement preparation and assessing the impact of this manipulation on behavioral performance. A further limitation of our study is that we do not unambiguously record the activity of identified interneuron subpopulations during movement onset. Such recordings could lend further support to the roles that we propose for PV+ and SOM+ interneurons in shaping ramping

signals. Furthermore, preparatory ramping signals have traditionally been studied in the context of delayed discrimination tasks. To test whether the proposed integration processes may underlie motor preparation signals more generally, it would be necessary to assess how membrane potential and spike ramping signals evolve during training in a go/no-go task, and how they depend on specific interneuron subpopulations (Gao et al., 2018; Inagaki et al., 2019; Murakami et al., 2014). Finally, to understand the unique contribution of MOs to multisensory integration processes preceding motion, it would be interesting to compare pre-motor signals in MOs with those in other neighboring regions, such as medial prefrontal cortex or primary motor cortex.

ACKNOWLEDGMENTS

We thank Ian Duguid and Josh Dacre for comments on the manuscript. We thank Lucile Le Chevalier-Sontag and Claire Lecestre for their technical support. This work was supported by grants from the ERC (StG 678790 NEWRON to C.S.-H., MSCA 800027 FindMEMO to M.A., Human Brain Project SGA2 785907 to J.-P.C. and F.K., and Human Brain Project SGA3 945539 to J.-P.C.), the Pasteur Weizmann Council (C.S.-H.), the INCEPTION program (Investissement d'Avenir grant ANR-16-CONV-0005 to C.O.), and a Pasteur-Roux fellowship to M.A.. Schematic drawings in the graphical abstract and in Figure 2 were adopted from <https://scidraw.io/> under a creative commons license (CC-BY).

AUTHOR CONTRIBUTIONS

Conceptualization: C.L.Z., J.-P.C., and C.S.-H.; methodology: C.L.Z., C.S.-H., F.K., and M.A.; experiments: C.L.Z.; data analysis and investigation: C.L.Z., H.L.K., C.O., and C.S.-H.; computational modelling: C.S.-H.; resources: U.M. and C.S.-H.; writing – original draft: C.L.Z. and C.S.-H.; writing – review & editing: C.L.Z., F.K., M.A., C.O., U.M., J.-P.C., and C.S.-H.; supervision, C.S.-H.; funding acquisition, C.S.-H., M.A., J.-P.C., and F.K..

DECLARATION OF INTERESTS

The authors declare no competing interests.

MAIN FIGURES

Figure 1. Role of MOs in a goal-directed behavioral VR task.

(A) Top, illustration of the virtual-reality (VR) environment. Bottom, schematic drawing of the goal-directed go/no-go task.

(B-C) Training performance quantified as reward rate (B, dispensed rewards per completed lap) and success rate (C, successful licks ("hits") per dispensed reward). In each panel, the left graph shows training performance across days, the right graph compares training performance on day 1 vs day 6 (reward rate: day 1, 0.31 ± 0.04 vs day 6, 0.47 ± 0.05 rewards/lap; success rate: day 1, 0.31 ± 0.05 vs day 6, 0.55 ± 0.05 hits/reward; $n = 20$ mice).

(D-E) Example training sessions from the same mouse under control conditions (D) and after muscimol application the next day (E). Top traces show animal speed, bottom traces show animal position on the virtual-reality track, green drops indicate dispensed rewards, blue triangles indicate licks. The reward zone is located between 1.2–1.4 m along the track (green shaded region).

(F) A fluorescent marker (bodipy, 350 nL per site) was injected bilaterally at the same coordinates as muscimol ($0.6 \mu\text{g}/\mu\text{L}$, 350 nL per site). Left, coronal sections at different rostro-caudal levels from an example animal. Right, Cannula tip positions (bilateral injections into $n = 5$ mice, indicated in a single hemisphere as red circles) and example coronal section showing fluorescence signal where bodipy and muscimol were injected.

(G-H) Summary of performance in the goal-directed task before, during and after inactivation of MOs, as quantified by the reward rate (G) and the success rate (H) (reward rate: day before 0.46 ± 0.14 vs muscimol 0.07 ± 0.02 vs day after 0.37 ± 0.17 rewards/lap; success rate: day before 0.49 ± 0.14 vs muscimol 0.07 ± 0.07 vs day after 0.48 ± 0.12 hits/reward; $n = 5$ mice).

(I-L) Summary of running period frequency (I) and duration (J), and resting period frequency (K) and duration (L) before, during and after inactivation of MOs by local muscimol application. Running frequency (I): day before, 2.1 ± 0.4 , vs muscimol, 1.0 ± 0.2 , vs day after, 2.3 ± 0.2 periods/min; running duration: day before, 7.0 ± 1.2 , vs muscimol, 16.0 ± 6.9 , vs day after, 7.8 ± 0.9 seconds; resting frequency: day before, 4.3 ± 0.6 , vs muscimol, 4.2 ± 0.3 , vs day after, 4.8 ± 0.6 periods/min; resting duration: day before, 4.0 ± 0.3 , vs muscimol, 7.9 ± 0.5 , vs day after, 4.7 ± 0.3 seconds).

Error bars represent s.e.m. Statistical significance was assessed using repeated measures ANOVA (B, C, G-L), and Wilcoxon signed rank tests (B, C) for day 1 vs day 6. ns, not significant; $*p < 0.05$; $**p < 0.01$; $***p < 0.001$. Statistic values are provided in Table S1.

Figure 2. Distinct intrinsic membrane properties of superficial and deep MOs principal neurons in vivo.

(A) Schematic drawing of the recording set-up.

(B) Recording coordinates.

(C) Left, coronal section of frontal cortex indicating the recording region in MOs (labeled by extracellular injection of tdTomato); right, biocytin-filled MOs principal neurons.

(D) Distribution of recording depths ($n = 24$ superficial neurons, $n = 23$ deep neurons).

(E) Deep MOs principal neurons show a more depolarized baseline membrane potential (V_m) compared to superficial principal neurons.

(F) No significant difference in input resistance between deep and superficial MOs principal neurons.

(G) Left, Example V_m responses to sustained current injections. Right, relationship between firing rate and current injection (f-I curve). Deep neurons are more excitable than superficial neurons when large currents are injected (comparison between superficial and deep groups: $F = 9.94$, $p = 0.002$; comparison of two groups at 300 pA: $p = 0.01$).

Error bars represent s.e.m. Statistical significance was assessed using Mann-Whitney tests (E-F), and two-way ANOVA with Bonferroni post-hoc tests (G). ns, not significant; $*p < 0.05$; $**p < 0.01$. Mean values, s.e.m., and statistics details are provided in Table S1.

Figure 3. Differences in subthreshold membrane potential and firing rates between resting and running periods in MOs neurons.

(A) Experimental timeline for spontaneously running control mice (top) and mice trained in the goal-directed task (bottom).

(B-D) Comparison of the mean running speeds (B), duration of individual running periods (C), and rate of running periods (D) between recordings from the control and trained groups (mean speed: control 13.1 ± 1.4 vs trained 21.8 ± 1.7 cm/s; running period duration 10.8 ± 1.4 vs 7.7 ± 0.9 s; running frequency: control 0.6 ± 0.1 vs trained 1.1 ± 0.3 periods per minute; $n = 29$ for control and $n = 18$ for trained groups). Symbols represent individual recordings.

(E) Example whole-cell recording from a superficial MOs neuron during goal-directed behavior. Traces show (from top) animal speed, membrane potential (V_m), V_m after blanking action potentials, and V_m variance. Vertical dashed lines indicate movement onset.

(F) Same recording as in (E), with data aligned to the onset of running periods at $t = 0$ s. Traces show (from top) animal speed, membrane potential (V_m), low-pass filtered V_m after blanking action potentials, and V_m variance. Thin traces represent individual running periods, thick traces represent the mean across running periods. The thick trace on top of V_m (second from top) represents the mean of low-pass filtered V_m after blanking action potentials.

(G-J) Summary of firing rates (G), mean V_m (H), membrane potential difference (ΔV_m) between running and resting periods (I), and V_m variance (J) during resting (blue) and running periods (red), for recordings from the control group ($n = 29$ recordings) and from the group of mice trained ($n = 18$) in a goal-directed task (H, left: control group: resting -58.0 ± 1.5 mV vs running -56.0 ± 1.5 mV; H, right: trained group: resting -57.0 ± 1.7 mV vs running -51.9 ± 1.8 mV; I: control group: 1.98 ± 0.65 mV; trained group: 5.04 ± 0.87 mV; J, left: resting 26.5 ± 3.0 mV² vs running 9.5 ± 2.2 mV²; right: resting 32.2 ± 6.5 mV² vs running 9.0 ± 1.2 mV²).

Error bars represent \pm s.e.m. Statistical significance was assessed using Wilcoxon signed rank tests (G, H and J) for paired groups, and Mann-Whitney tests (B-D, and G-J) for unpaired groups. ns, not significant; * $p < 0.05$; ** $p < 0.01$; *** $p < 0.001$. Mean values, s.e.m., and statistics details are provided in Table S1. See also Figures S1–S6.

Figure 4. Task dependence of membrane potential and firing rate dynamics preceding movement onset.

(A-B) Example whole-cell recordings from different MOs neurons preceding movement onset at $t = 0$ s (indicated by a red vertical dashed line and an arrow). Thin blue traces represent raw membrane potential, thick traces represent low-pass filtered membrane potential after blanking action potentials. Note slower dynamics of depolarizing ramps in control animals (A) compared to trained animals (B).

(C-D) Summary of speed, membrane potential and firing rate dynamics preceding movement onset across control animals (C, $n = 11$ recordings) and trained animals (D, $n = 10$ recordings). Data are aligned to running onset at $t = 0$ s (indicated by a red vertical dashed line). Top, mean animal speed. Middle, mean membrane potential (thin traces), mean low-pass filtered membrane potential (thick traces, shaded regions represent mean \pm s.e.m). Bottom, thick traces represent mean spike firing rates (black), and mean of shuffled firing rates (grey, $n = 100$ shuffles). Shaded regions represent mean \pm s.e.m. Ticks represent spike firing, with all running periods of a single recording shown in a single row.

Statistical significance was assessed by Spearman's correlation (C-D). ns, not significant; * $p < 0.05$; ** $p < 0.01$; *** $p < 0.001$. Statistics details are provided in Table S1. See also Figures S3, S4 and S6.

Figure 5. Inactivation of local PV+ and SOM+ interneurons has differential effects on movement-related membrane potential and firing rate dynamics.

(A) Schematic drawing of the experimental paradigm. Control recordings are the same as those shown in Figure 3.

(B) Fluorescence image of H4MDi-mCherry-expressing SOM+ interneurons in a coronal slice of MOs.

(C) Example intracellular recording from a MOs neuron during chemogenetic inactivation of PV+ interneurons. Traces show (from top) animal speed, membrane potential (V_m), and V_m variance.

(D–F) Comparison of firing rates (D), mean membrane potential (E), and V_m variance (F) under control conditions ($n = 29$) and during chemogenetic inactivation of PV+ ($n = 28$) or SOM+ ($n = 34$) interneurons during resting periods (D: control conditions represent the same data as shown in Figure 3G, left, rest; during PV+ inactivation: 0.82 ± 0.11 Hz; during SOM+ inactivation: 0.63 ± 0.17 Hz; E: control conditions represent the same data as shown in Figure 3H, left, rest; during PV+ inactivation: -58.1 ± 1.3 mV; during SOM+ inactivation: -60.6 ± 1.1 mV; F: control conditions represent the same data as shown in Figure 3J, left, rest; during PV+ inactivation: 45.1 ± 4.3 mV²; during SOM+ inactivation: 35.6 ± 3.6 mV²).

(G–J) Comparison of firing rates (G), membrane potential (H), changes in membrane potential (I), and V_m variance (J) during resting (blue) and running periods (red) under control conditions ($n = 29$) and during chemogenetic inactivation of PV+ ($n = 14$), or SOM+ interneurons ($n = 12$). Recordings in G–J represent recordings in D–F with running periods. (G: control conditions represent the same data as in Figure 3G, left; during PV+ inactivation: resting 0.86 ± 0.14 Hz vs running 2.77 ± 1.02 Hz; during SOM+ inactivation: resting 0.71 ± 0.33 Hz vs running 2.07 ± 1.10 Hz; H: control conditions represent the same data as shown in Figure 3H; PV+ inactivation: resting -60.3 ± 1.4 mV vs running -53.0 ± 2.2 mV; SOM+ inactivation: resting -61.8 ± 1.7 mV vs running -58.3 ± 2.7 mV; I: control conditions represent the same data as shown in Figure 3I, left; PV+ inactivation: 7.3 ± 1.4 mV; SOM+ inactivation: 3.5 ± 2.0 mV; J: control conditions represent the same data as shown in Figure 3J, left; PV+ inactivation: resting 39.9 ± 7.2 mV² vs running 15.9 ± 4.0 mV²; SOM+ inactivation: resting 37.2 ± 5.7 mV² vs running 23.1 ± 5.8 mV²).

Error bars represent \pm s.e.m. Statistical significance was assessed using Kruskal-Wallis tests (D–F and I), Wilcoxon signed rank tests (G, H, I and K) for paired groups, and Mann-Whitney tests (G) for unpaired groups. ns, not significant; * $p < 0.05$; ** $p < 0.01$; *** $p < 0.001$. Mean values, s.e.m., and statistics details are provided in Table S1. See also Figure S7.

Figure 6. Activity of local PV+ and SOM+ interneurons in MOs differentially shape subthreshold membrane potential ramps.

(A–B) Example whole-cell recordings from different MOs neurons preceding movement onset at $t = 0$ s (indicated by a red vertical dashed line and an arrow) during chemogenetic inactivation of PV+ interneurons (A) or of SOM+ interneurons (B). Thin blue traces represent raw membrane potential, thick traces represent low-pass filtered membrane potential.

(C–D) Summary of speed, membrane potential and firing rate dynamics preceding movement onset during chemogenetic inactivation of PV+ interneurons (C, $n = 8$ recordings) or of SOM+ interneurons (D, $n = 7$ recordings). Data are aligned to running onset at $t = 0$ s (indicated by a red vertical dashed line). Top, mean animal speed. Middle, mean membrane potential (thin traces), mean low-pass filtered membrane potential (thick traces, shaded regions represent mean \pm s.e.m). The black dash traces represent the control recordings ($n = 11$ spiking neurons, same as shown in Figure 4C). Bottom, thick traces represent mean spike firing rates (orange and brown), and mean of shuffled firing rates (grey, $n = 100$ shuffles). Shaded regions represent mean \pm s.e.m. Ticks represent spike firing, with each row showing a different recording.

Statistical significance was assessed by Spearman’s correlation. ns, not significant; * $p < 0.05$; ** $p < 0.01$; *** $p < 0.001$. Statistics details are provided in Table S1. See also Figure S7.

Figure 7. Concerted action of external inputs and local SOM+ and PV+ interneurons drives task-dependent ramping signals in a computational model of the local MOs circuit.

(A) Top, A simple computational model of the local MOs circuit with 3 units: SOM+ interneurons, PV+ interneurons, and principal neurons (PNs). All units receive the same external inputs. Bottom, simulation results. Activity in arbitrary units is plotted against time. External inputs (top) increase in a step-like fashion at $t = -10$ s before the onset of movement. By virtue of their recurrent

connectivity in conjunction with inhibitory inputs (middle), pyramidal cells (bottom) respond with a graded slow increase of activity.

(B) Simulation of chemogenetic inactivation of SOM+ interneurons. Absence of SOM+-mediated inhibition of PV+ interneurons leads to an increase in PV+ activity, thereby abolishing the ramp in pyramidal neurons.

(C) Simulation of chemogenetic inactivation of PV+ interneurons. Absence of inhibition from PV+ interneurons leads to an acceleration of ramping activity, and to an increase of baseline activity.

(D) Simulation of increasing excitatory synaptic weights on SOM+ interneurons. Increased activation of SOM+ interneurons leads to a change in SOM+/PV+ activity balance over time in favor of SOM+ interneurons, thereby accelerating the ramping activity in principal neurons.

See also Table S2.

MAIN TABLES AND LEGENDS

n.a.

STAR METHODS

KEY RESOURCES TABLE

REAGENT or RESOURCE	SOURCE	IDENTIFIER
Bacterial and virus strains		
AAV5.hSyn.DIO.hM4D(Gi).mcherry	Addgene	44362-AAV5
AAV1-CAG-FLEX-tdTomato-WPRE	Addgene	28306-AAV1
AAV1-CAG-tdTomato-WPRE	Addgene	59462-AAV1
Chemicals, peptides, and recombinant proteins		
Biocytin	Sigma-Aldrich	B4261
Potassium methanesulfonate	Sigma-Aldrich	83000
Potassium chloride	Sigma-Aldrich	P9333
Sodium chloride	Sigma-Aldrich	S9888
Magnesium chloride solution	Sigma-Aldrich	M1028
Calcium chloride solution	Sigma-Aldrich	21115
HEPES	Sigma-Aldrich	H3375
EGTA	Sigma-Aldrich	E3889
Adenosine 5'-triphosphate disodium salt hydrate	Sigma-Aldrich	A26209
Guanosine 5'-triphosphate sodium salt hydrate	Sigma-Aldrich	G8877
Phosphocreatine disodium salt hydrate	Sigma-Aldrich	P7936
BODIPY TMR-X	Invitrogen	D6117
Clozapine N-oxide dihydrochloride	Tocris Biosciences	Cat. No. 6329
Muscimol	Tocris Biosciences	Cat. No. 0289
Deposited data		
Analyzed data	This paper	N/A
Experimental models: Organisms/strains		
Mouse: C57BL/6J	Janvier Labs	SC-C57J-M4S
Mouse: PV-CRE	Jackson Laboratories	013044
Mouse: SOM-CRE	Jackson Laboratories	008069
Software and algorithms		
Python	https://www.python.org/	N/A
Blender	https://www.blender.org/	N/A
Prism	https://www.graphpad.com/	N/A
SpikeGLX	https://billkarsh.github.io/SpikeGLX/	N/A
Kilosort 2	https://github.com/MouseLand/Kilosort	N/A
DeepLabCut	https://github.com/DeepLabCut/DeepLabCut	
Phy	https://github.com/cortex-lab/phy	N/A
Simulation code	https://zenodo.org/record/5625822	10.5281/zenodo.5625822
Other		
Head post for head-fixed animals	Luigs & Neumann	200-200 500 2133-1-11-20
Neuropixel 1.0	IMEC (https://www.neuropixels.org/)	N/A

RESOURCE AVAILABILITY

Lead contact

Further information and requests for resources and reagents should be directed to and will be fulfilled by the Lead Contact, Christoph Schmidt-Hieber (christoph.schmidt-hieber@pasteur.fr).

Materials availability

This study did not generate new unique reagents.

Data and code availability

- All data reported in this paper will be shared by the lead contact upon request.
- All original code has been deposited at Zenodo and is publicly available as of the date of publication. The DOI is listed in the key resources table.
- Any additional information required to reanalyze the data reported in this paper is available from the lead contact upon request.

EXPERIMENTAL MODEL AND SUBJECT DETAILS

Mice

All procedures were carried out in accordance with the national guidelines on the ethical use of animals of EU Directive 2010/63/EU and were approved by the Ethics Committee CETEA of the Institut Pasteur (APAFIS#7771-2016112516084126 v1). 6- to 12-week-old wild-type (WT) C57BL/6J and transgenic mice were maintained at our animal facility on a regular 12/12h light-dark cycle with *ad libitum* access to food and water. The following Cre mouse lines were obtained from the Jackson Laboratories: SST-Cre (no: 013044) and PV-Cre (no: 008069). These mice were backcrossed onto a C57BL/6J background. Stereotaxic injections were performed in 6- to 8-week-old male mice.

METHOD DETAILS

Surgical procedures and viral vector transduction

Surgeries were performed under continuous anesthesia with isoflurane (5% for induction, 1–3% for maintenance, vol/vol). Preceding the surgery, mice were treated with buprenorphine (0.1 mg/kg i.p.) and lidocaine (0.4 mL/kg of a 1% solution, local application). Mice were positioned in a stereotaxic apparatus (David Kopf Instruments, Tujunga, CA). A half-circle stainless steel headpost (Luigs & Neumann) was fixed to the mouse skull using dental cement (Super-Bond, Sun Medical Co. Lt). Animals were allowed to recover for 2 weeks after head post implantation. Body temperature was monitored and maintained at 37°C by placing the animals on a heating

pad during and after the surgery. Animals were treated with metacam (1 mg/kg i.p.) before returning them to their home cages.

Circular craniotomies (0.5 mm diameter) were performed above the MOs under isoflurane anesthesia 1h before the onset of recordings using a dental drill (stereotaxic coordinates from Bregma, anteroposterior [AP] +2.7-3.1 mm, mediolateral [ML] \pm 0.4-1.0 mm). Animals were treated with an injection of metacam (1 mg/kg i.p.) at the end of the procedure, and then transferred to the recording setup.

To suppress the activity of PV+ or SOM+ interneurons, an adeno-associated viral vector (AAV5-hSyn-DIO-hM4D(Gi)-mCherry, ref Addgene-44362, 7E12 vector genomes (vg)/ml) was injected into the MOs of either PV-Cre or SOM-Cre mice. The adeno-associated viral vectors (AAV1-CAG-FLEX-tdTomato-WPRE, ref Addgene-28306, 1E13 vector genomes (vg)/ml) and (AAV1-CAG-tdTomato-WPRE, ref Addgene-59462, 5E12 vector genomes (vg)/ml) were used as control viruses. 6- to 8-week-old mice were injected with vectors (300~400 nL per site) into the MOs region (stereotaxic coordinates from Bregma, anteroposterior [AP] +2.7~3.1 mm, mediolateral [ML] \pm 0.4~0.6 mm, 2 injections at 300 μ m and 500 μ m depth from dura). The virus was bilaterally pressure-injected through glass pipettes (Drummond Wiretrol 10 μ l) using an oil-hydraulic micromanipulator (MO-10, Narishige, Japan) at a rate of 100 nL/min. Headpost implantation was performed 3 weeks after the injections. Before the recordings were performed, CNO (Tocris Biosciences; 5 mg/kg i.p.) was administered to activate the hM4D receptor 30 min prior to recordings (Jackson et al., 2018). All recordings were performed within 3 hours after CNO injection.

Behavioral training and analysis

Two weeks after the headpost implantation, mice were handled 10 minutes per day for 3 days. After this period, head-fixed mice were placed on a cylindrical polystyrene treadmill (20 cm diameter) supported by pressurized air bearings. Cylinder rotation associated with animal locomotion was read out from the surface of the treadmill with a computer mouse (G700s, Logitech, used in wired mode) at a poll rate of 1 kHz. As shown in Figure 1A, all mice were habituated to the treadmill 10-20 min per day for 2 consecutive days. Following habituation, mice were trained 30-45 min per day for 2-3 days to perform self-paced voluntary movement on the treadmill in a dark environment.

Another group of mice was trained in a goal-directed task in a virtual-reality environment. The virtual reality setup was implemented as described previously (Schmidt-Hieber and Häusser, 2013). Briefly, motion on the treadmill was read out as described above and linearly converted to

one-dimensional movement along the virtual reality corridor. The virtual environment was projected onto a spherical dome screen (120 cm diameter), covering nearly the entire field of view of the animal, using a quarter-sphere mirror (45 cm diameter) and a projector (Casio XJ-A256) located below the mouse. The virtual linear corridor was 1.2 m long, enriched with objects placed along the linear track and vertical or oblique grating textures on the walls. A reward zone was located at the end (1.0-1.1 m) of the corridor. The Blender Game Engine (<http://www.blender.org>) was used in conjunction with the Blender Python API to drive the virtual reality system. Controlled water delivery was used to improve animal motivation during the goal-directed task. At the beginning of experiments, mice were placed under controlled water supply (0.5 mg of hydrogel per day, Clear H₂O, BioService) and maintained at ~85% of their initial body weight over the course of behavioral training and electrophysiology experiments. The welfare and weight of animals were checked and documented on a daily basis. After habituation and water deprivation, mice underwent 6 training sessions, 30-45 min each, over the course of 1 week before recordings (Figures 1A-1C). A drop of sugar water (10 μ l, 8 mg/mL sucrose) was dispensed by a spout as a reward if they spent 2 s or more within the reward zone. Animal licking was detected with a piezo element attached to the reward spout. A “hit” was detected when the animal performed at least two licks within a period of 2 seconds before or 2 seconds after the reward delivery. When the animals reached the end of the linear track, they were “teleported” back to the start of the virtual corridor after crossing a black frontal wall, indicating the end of a lap and the onset of the subsequent one. Behavioral performance of the training group was comparable between different sessions (Figures 1A-1C). Locomotor behavior was analyzed during muscimol application (Figures 1E-1L) and comparable between the trained group and the spontaneously running group (Figures 3B-3D).

To detect whisker and body motion (Figure S4), we filmed the animal using an infrared-sensitive camera (Point Grey CM3-U3-13Y3M-CS) operating at a frame rate of 200 Hz. The animal was illuminated by an array of infrared LEDs. Whisker movements were analyzed with the markerless pose estimation software DeepLabCut (Mathis et al., 2018). The bases and tips of 4 whiskers, i.e. a total of 8 labels, were identified across all captured frames (Figure S4A). To quantify whisker movement, across all captured frames we computed the sum of the Euclidean distances, in units of pixels, that were covered by each of the 8 whisker labels between adjacent frames. A whisker motion index was obtained by z-scoring the data, subtracting any offset, and low-pass filtering at $f_c \sim 0.1$ Hz. Onset of whisker movement preceding onset of running were detected where the whisker motion index continuously exceeded 10% of its maximal value within a time window of

15 s before running onset (Figure S4C). During muscimol application, the whisker movement period frequency per second was analyzed (Figures S4G-S4H).

Cannula implantation for muscimol Infusion

To infuse muscimol into MOs, two stainless steel guide cannulae (26 gauge; PlasticsOne, Roanoke, VA) were bilaterally implanted above the MOs (from Bregma position, anteroposterior [AP] +2.6–3.1 mm, mediolateral [ML] \pm 0.8–1.3 mm, angled at 25–30° towards medial from vertical; dorsoventral, 0.5 mm). Cannulae were anchored to the skull with dental cement (Super-Bond, Sun Medical Co. Lt). Body temperature was monitored and maintained at 37°C by placing the animals on a heating pad during and after the surgery, and the guides were covered with a dummy cannula to reduce the risk of infection. Mice were allowed to recover during 3–4 weeks from surgery before the start of water restriction, and their well-being and weight were assessed on a daily basis.

An infusion cannula (33 gauge; connected to a 1 μ L Hamilton syringe via polyethylene tubing) was inserted through the guide cannula, protruding 0.5 mm, to target the MOs. Muscimol (0.6 μ g/ μ L in saline, 350 nL per site) was infused bilaterally at a rate of 100 nL per min using a motorized pump (Legato 100, Kd Scientific Inc., Hilliston, MA), 45–60 min before behavioral testing. To allow for penetration of the drug, the injector was maintained in position for an additional 3 min after the end of the infusion. Mice were placed back in their home cages at the end of the injection procedure.

To analyze the location and extent of the injections, we injected the fluorophore BODIPY TMR-X into MOs (Invitrogen; 5 mM in PBS 0.1 M, DMSO 40%). After 3 hours, animals were deeply anaesthetized and brains were fixed by intracardiac perfusion with paraformaldehyde (4% in PBS). Slices (50 μ m) were cut with a vibratome and imaged using a confocal microscope (Opterra, Bruker). Mice were considered for further analysis if fluorescence signals could be confirmed in MOs (Figure 1F).

***In vivo* patch-clamp electrophysiology**

Whole-cell patch-clamp recordings were performed from head-fixed mice placed on the treadmill as described above. Glass pipettes were pulled from borosilicate glass (~5 M Ω pipette resistance) and filled with internal solution containing (in mM) 130 potassium methanesulphonate, 7.0 KCl, 0.3 MgCl₂, 0.1 EGTA, 10 HEPES, 1 sodium phosphocreatine, 3.0 Na₂ATP, 0.3 NaGTP. 5 mg/ml biocytin was added to the internal solution for staining purposes. pH was adjusted to 7.2 with KOH. Osmolarity was 289 mOsm. Whole-cell patch-clamp recordings were obtained using a

standard blind-patch approach (Margrie et al., 2002; Schmidt-Hieber and Häusser, 2013). In brief, a high positive air pressure (~1000 mbar) was applied to the pipettes before slowly lowering them into the dorsal part of the MOs region (Figure 2B) via a small craniotomy (~500 μ m) using a micromanipulator (Luigs & Neumann Mini In Vivo). Recordings were obtained at a depth of 150-420 μ m (superficial neurons; typically layers 2/3) or 430-850 μ m (deep neurons; typically layers 4-6) from the pial surface (Figure 2D). At a depth of ~150 μ m from the brain surface, the air pressure was decreased to 50~80 mbar. Seal resistances were always \gg 1 G Ω , and access resistances were typically 25~70 M Ω , with recordings terminated when access resistance exceeded 100 M Ω . Recordings were made in current-clamp mode, and no holding current was applied during recordings.

Membrane potential was low-pass filtered at 10 kHz and acquired at 50 kHz (Intan Technologies CLAMP system). During recordings, a silver/silver chloride reference electrode (0.3 mm diameter) was positioned in an additional small craniotomy close to lambda. An external solution containing (in mM) 150 NaCl, 2.5 KCl, 10 HEPES, 2 CaCl₂, and 1 MgCl₂ (pH 7.2, 289 mOsm) was perfused on top of the craniotomy through a round plastic chamber (4 mm diameter).

***In vivo* extracellular electrophysiology**

Extracellular recordings of population activity were made using Neuropixels probes (Jun et al., 2017). Probes were lowered into the dorsal part of the MOs region to a depth of ~2.0mm measured from the brain surface via a small craniotomy (~500 μ m) at an angle of 15° from vertical using a micromanipulator (Sensapex uMp-4). A silver/silver chloride wire, which was soldered to the external reference of the probes and connected to ground, was positioned in an additional small craniotomy. Recordings were performed from head-fixed mice placed on the treadmill as described above. Electrophysiological data were recorded with SpikeGLX (<https://billkarsh.github.io/SpikeGLX/>) and signals from the AP channels (0.3-10 kHz bandwidth, sampling rate of 30 kHz) were used for further processing. Spike sorting for unit identification was performed with Kilosort 2 (<https://github.com/MouseLand/Kilosort>). Identified units were manually curated using Phy (<https://github.com/cortex-lab/phy>). Putative cell types were assessed based on peak-to-valley ratio and half-valley width of the spike waveforms for each neuron by fitting a Gaussian mixture model (Kim et al., 2016b; Stark et al., 2013). Units with low classification confidence ($P < 0.95$) were unassigned. The interneuron population was further split based on average firing rate: interneurons with a mean firing rate > 10 Hz were classified as fast-spiking interneurons (Figure S3).

Immunohistochemistry and cell identification

At the end of some recordings, mice were deeply anesthetized with an overdose of ketamine/xylazine (100 mg/kg and 10 mg/kg i.p.) and quickly perfused transcardially with 0.1 M phosphate-buffered saline followed by paraformaldehyde (4% in PBS). Brains were removed from the skull and kept in PFA for at least 24 h. We stained 50- μ m-thick parasagittal slices with Alexa Fluor 488–streptavidin to reveal biocytin-filled neurons and patch pipette tracts. We identified neurons as principal cells according to their characteristic electrophysiological signature (Figure 2G), including the presence of frequency adaptation during spike trains, and absence of pronounced afterhyperpolarizations following action potentials (Zhao et al., 2016). Whenever the morphological recovery of recorded neurons was successful, we confirmed this classification using the shape and position of biocytin-filled neurons. In addition, the pipette tract was confirmed to terminate in MOs (Figure 2C).

QUANTIFICATION AND STATISTICAL ANALYSIS

***In vivo* whole-cell electrophysiology data analysis**

Input resistance was calculated from the steady-state voltage response to a small hyperpolarizing 500-ms current pulse from baseline membrane potential (Figure 2G). Only data from mice that were resting during this period were used (speed < 0.5 cm/s). Baseline membrane potential was measured before current pulse injections at the beginning of the recording. Spontaneous firing rate and membrane potential were measured across recordings with durations exceeding 60s. To analyze subthreshold membrane potential and its variance, traces were digitally low-pass filtered at 5 kHz and resampled at 10 kHz. Action potentials were then removed by thresholding to determine action potential times and then masking values 2 ms before and 10-20 ms after the action potential peak. Membrane potential oscillations were analyzed by bandpass-filtering membrane potential traces after removal of action potentials (Figure S2). Power spectra were computed from subthreshold membrane potential traces using Hanning windowing over data windows of 215 sampling points (~328 ms). Membrane potential variance time series were computed in rolling time windows with a width of 1000 ms.

Changes in subthreshold membrane potential (ΔV_m) were computed by subtracting the mean of subthreshold membrane potential traces after spike removal (see above). To compute movement-aligned mean traces of ΔV_m (Figures 4, 6 and S6-S7), we aligned traces to movement periods spanning 15 seconds before movement onset until 5 seconds after movement onset. After alignment, we computed the mean of each trace between 15 and 10 seconds before the onset of movement, and subtracted this baseline from each trace.

Data inclusion criteria

For the analysis of intrinsic membrane properties (Figures 2E-2G), cells that met basic recording criteria (initial access resistance < 70 M Ω , initial baseline membrane potential < -50 mV) from the control group of mice were included (47 neurons). For the analysis of firing rate and V_m dynamics (Figures 3-6 and S5-S7), only cells with recording durations exceeding 60 s were included. Typical recordings with animals resting and running on the treadmill lasted 5–10 min, and longer recordings (~30 min) were occasionally achieved.

Running periods were defined as time intervals when the running speed continuously exceeded 1 cm/s during at least 2 s. This criterion was confirmed by visual inspection of each recording to avoid inclusion of short or fractionated running periods. When we aligned data to the onset of movement (Figures 4, 6, S6 and S7), running periods had to be preceded by resting periods with a duration >10s to ensure that the pre-movement period was not contaminated by movement. Furthermore, the recording duration after movement onset had to exceed 5 s. These criteria were applied to 29 recordings during spontaneous movement and 18 recordings during goal-directed movement (Figure 3 and S5), reducing the number of recordings to 23 (12 superficial and 11 deep recordings) for the control group, and 12 (5 superficial and 7 deep recordings) for the trained group of animals (Figure S6). In our analysis of pre-movement spike firing (Figures 4 and 6), additional criteria were applied as we only selected neurons that spontaneously fired spikes during the movement-aligned time period. This selection further reduced the number of recordings to 11 out of 23 during spontaneous movement, and 10 out of 12 during goal-directed movement (Figure 4). In Figures 6 and S7, we selected recordings with resting periods >6 s preceding movement onset and recording durations > 5 s after movement onset. This selection further reduced the number of recordings to 8 out of 14 during PV+ interneurons inactivation, and 7 out of 12 during SOM+ interneurons inactivation (Figure 5).

Spike rates in whole-cell recordings were computed from the time points of action potential peaks (see above) in time bins of 500 ms and filtered using a sliding average with a width of 3 s. Shuffled spike rate data were obtained by generating 100 artificial data sets. Each artificial data set was created from the original data set by shifting it circularly by a random number of sampling points. To quantify membrane potential ramps, we computed the mean of ΔV_m values for each recording in time bins of 1 s in movement-aligned ΔV_m traces (see above). Across all binned values of all recordings, we then computed the Spearman rank correlation to test for significant monotonous increases in membrane potential. To quantify the temporal dynamics of membrane potential and spike ramps, Spearman rank correlations were computed for different time periods preceding

onset of movement and during movement, as indicated in the figures and figure legends (Figures 4, 6, S6 and S7).

Statistical analysis

Wilcoxon signed-rank or Mann-Whitney U tests were used to assess the statistical significance of paired or unpaired data as appropriate. For multiple comparisons, we performed Kruskal-Wallis tests and adjusted using Dunn's correction. In Figures 1B-1C, 1G-1L, S4D and S4H, repeated measures ANOVA was applied. In Figures 2G, S6F, S6I, S7C and S7D, a two-way ANOVA with factors' interactions and Bonferroni post-hoc tests were used. Spearman rank correlations were computed to assess the significance of ramping dynamics (see above; Figures 4, 6, S6 and S7). Statistics details are listed in Table S1. Tests were considered significant if the p value was < 0.05 , otherwise "n.s." denotes "not significant". Bar graphs and error bars show mean \pm s.e.m..

Computational modelling

To simulate neuronal activity preceding onset of movement, we developed a reduced model of the local MOs circuit consisting of 3 neurons: a SOM+ cell, a PV+ cell, and a principal neuron. The dynamics of the rate-based model neurons was defined by

$$\tau_i \frac{ds_i}{dt} + s_i = \sum_j w_{ji} f(s_j),$$

where τ_i is the time constant of neuronal integration of neuron i , s_i and s_j are the activities of neurons i and j , dt is the simulation time step, and w_{ji} is the synaptic weight of inputs from neuron j to neuron i . $f(x)$ is a threshold function: $f(x) = x$ for $x > 0$, and $f(x) = 0$ otherwise. All 3 neurons received input from an external source representing thalamocortical inputs. Weights of synaptic connections between neurons were adjusted to reflect our experimental results (see Table S2). Time constants for neuronal integration τ_i were set to 20 ms for both interneurons and to 40 ms for the principal neuron. The simulation time step was set to 0.5 ms. Ramping activity preceding the onset of running ($t = 0$ s) was simulated by increasing the activity of the external inputs in a step-like fashion at $t = -10$ s. Chemogenetic inactivation of PV+ or SOM+ interneurons were simulated by fixing the activities of the corresponding model neurons to 0 throughout the simulation. Plasticity of SOM+ interneurons was simulated by increasing the excitatory synaptic weights to the SOM+ model interneuron (see Table S2).

SUPPLEMENTAL EXCEL TABLE

Table S1. Analysis and statistics details. Related to STAR Methods.

REFERENCES

- Ährlund-Richter, S., Xuan, Y., van Lunteren, J.A., Kim, H., Ortiz, C., Pollak Dorocic, I., Meletis, K., and Carlén, M. (2019). A whole-brain atlas of monosynaptic input targeting four different cell types in the medial prefrontal cortex of the mouse. *Nat. Neurosci.* 22, 657–668.
- Barthas, F., and Kwan, A.C. (2017). Secondary Motor Cortex: Where “Sensory” Meets “Motor” in the Rodent Frontal Cortex. *Trends Neurosci.* 40, 181–193.
- Bennett, C., Arroyo, S., and Hestrin, S. (2013). Subthreshold mechanisms underlying state-dependent modulation of visual responses. *Neuron* 80, 350–357.
- Biane, J.S., Takashima, Y., Scanziani, M., Conner, J.M., and Tuszynski, M.H. (2016). Thalamocortical Projections onto Behaviorally Relevant Neurons Exhibit Plasticity during Adult Motor Learning. *Neuron* 89, 1173–1179.
- Bureau, I., von Saint Paul, F., and Svoboda, K. (2006). Interdigitated paralemniscal and lemniscal pathways in the mouse barrel cortex. *PLoS Biol.* 4, e382.
- Buzsáki, G., and Draguhn, A. (2004). Neuronal oscillations in cortical networks. *Science* 304, 1926–1929.
- Chaudhuri, R., and Fiete, I. (2016). Computational principles of memory. *Nat. Neurosci.* 19, 394–403.
- Chen, T.-W., Li, N., Daie, K., and Svoboda, K. (2017). A Map of Anticipatory Activity in Mouse Motor Cortex. *Neuron* 94, 866–879.e4.
- Churchland, M.M., Yu, B.M., Cunningham, J.P., Sugrue, L.P., Cohen, M.R., Corrado, G.S., Newsome, W.T., Clark, A.M., Hosseini, P., Scott, B.B., et al. (2010a). Stimulus onset quenches neural variability: a widespread cortical phenomenon. *Nat. Neurosci.* 13, 369–378.
- Churchland, M.M., Cunningham, J.P., Kaufman, M.T., Ryu, S.I., and Shenoy, K.V. (2010b). Cortical preparatory activity: representation of movement or first cog in a dynamical machine? *Neuron* 68, 387–400.
- Coen, P., Sit, T.P.H., Wells, M.J., Carandini, M., and Harris, K.D. (2021). Mouse frontal cortex mediates additive multisensory decisions. *bioRxiv* 2021.04.26.441250.
- Cottam, J.C.H., Smith, S.L., and Häusser, M. (2013). Target-specific effects of somatostatin-expressing interneurons on neocortical visual processing. *J. Neurosci.* 33, 19567–19578.
- Courtin, J., Chaudun, F., Rozeske, R.R., Karalis, N., Gonzalez-Campo, C., Wurtz, H., Abdi, A., Baufreton, J., Bienvenu, T.C.M., and Herry, C. (2014). Prefrontal parvalbumin interneurons shape neuronal activity to drive fear expression. *Nature* 505, 92–96.
- Cummings, K.A., and Clem, R.L. (2020). Prefrontal somatostatin interneurons encode fear memory. *Nat. Neurosci.* 23, 61–74.
- Dacre, J., Colligan, M., Clarke, T., Ammer, J.J., Schiemann, J., Chamosa-Pino, V., Claudi, F., Harston, J.A., Eleftheriou, C., Pakan, J.M.P., et al. (2021). A cerebellar-thalamocortical pathway drives behavioral context-dependent movement initiation. *Neuron* 109, 2326–2338.

- DeFelipe, J., and Fariñas, I. (1992). The pyramidal neuron of the cerebral cortex: morphological and chemical characteristics of the synaptic inputs. *Prog. Neurobiol.* 39, 563–607.
- Donoghue, J.P., and Wise, S.P. (1982). The motor cortex of the rat: cytoarchitecture and microstimulation mapping. *J. Comp. Neurol.* 212, 76–88.
- Ebbesen, C.L., Insanally, M.N., Kopec, C.D., Murakami, M., Saiki, A., and Erlich, J.C. (2018). More than Just a “Motor”: Recent Surprises from the Frontal Cortex. *J. Neurosci.* 38, 9402–9413.
- Economo, M.N., Viswanathan, S., Tasic, B., Bas, E., Winnubst, J., Menon, V., Graybiel, L.T., Nguyen, T.N., Smith, K.A., Yao, Z., et al. (2018). Distinct descending motor cortex pathways and their roles in movement. *Nature* 563, 79–84.
- Eggermann, E., Kremer, Y., Crochet, S., and Petersen, C.C.H. (2014). Cholinergic signals in mouse barrel cortex during active whisker sensing. *Cell Rep.* 9, 1654–1660.
- Erlich, J.C., Bialek, M., and Brody, C.D. (2011). A cortical substrate for memory-guided orienting in the rat. *Neuron* 72, 330–343.
- Erlich, J.C., Brunton, B.W., Duan, C.A., Hanks, T.D., and Brody, C.D. (2015). Distinct effects of prefrontal and parietal cortex inactivations on an accumulation of evidence task in the rat. *eLife* 4, e05457
- Fino, E., and Yuste, R. (2011). Dense inhibitory connectivity in neocortex. *Neuron* 69, 1188–1203.
- Fuster, J.M., and Alexander, G.E. (1971). Neuron Activity Related to Short-Term Memory. *Science* 173, 652–654.
- Gabbott, P.L.A., Warner, T.A., Jays, P.R.L., Salway, P., and Busby, S.J. (2005). Prefrontal cortex in the rat: projections to subcortical autonomic, motor, and limbic centers. *J. Comp. Neurol.* 492, 145–177.
- Gao, Z., Davis, C., Thomas, A.M., Economo, M.N., Abrego, A.M., Svoboda, K., De Zeeuw, C.I., and Li, N. (2018). A cortico-cerebellar loop for motor planning. *Nature* 563, 113–116.
- Gentet, L.J., Avermann, M., Matyas, F., Staiger, J.F., and Petersen, C.C.H. (2010). Membrane potential dynamics of GABAergic neurons in the barrel cortex of behaving mice. *Neuron* 65, 422–435.
- Gilbert, C.D., and Sigman, M. (2007). Brain States: Top-Down Influences in Sensory Processing. *Neuron* 54, 677–696.
- Goard, M.J., Pho, G.N., Woodson, J., and Sur, M. (2016). Distinct roles of visual, parietal, and frontal motor cortices in memory-guided sensorimotor decisions. *Elife* 5, e13764.
- Goldman-Rakic, P.S. (1995). Cellular basis of working memory. *Neuron* 14, 477–485.
- Guo, Z.V., Li, N., Huber, D., Ophir, E., Gutnisky, D., Ting, J.T., Feng, G., and Svoboda, K. (2014). Flow of Cortical Activity Underlying a Tactile Decision in Mice. *Neuron* 81, 179–194.
- Guo, Z.V., Inagaki, H.K., Daie, K., Druckmann, S., Gerfen, C.R., and Svoboda, K. (2017).

- Maintenance of persistent activity in a frontal thalamocortical loop. *Nature* 545, 181–186.
- Hanes, D.P., and Schall, J.D. (1996). Neural Control of Voluntary Movement Initiation. *Science* 274, 427–430.
- Hangya, B., Pi, H.-J., Kvitsiani, D., Ranade, S.P., and Kepecs, A. (2014). From circuit motifs to computations: mapping the behavioral repertoire of cortical interneurons. *Curr. Opin. Neurobiol.* 26, 117–124.
- Harris, K.D., and Thiele, A. (2011). Cortical state and attention. *Nature Reviews Neuroscience* 12, 509–523.
- Hu, H., Gan, J., and Jonas, P. (2014). Interneurons. Fast-spiking, parvalbumin⁺ GABAergic interneurons: from cellular design to microcircuit function. *Science* 345, 1255263.
- Inagaki, H.K., Fontolan, L., Romani, S., and Svoboda, K. (2019). Discrete attractor dynamics underlies persistent activity in the frontal cortex. *Nature* 566, 212–217.
- Jackson, J., Karnani, M.M., Zemelman, B.V., Burdakov, D., and Lee, A.K. (2018). Inhibitory Control of Prefrontal Cortex by the Claustrum. *Neuron* 99, 1029–1039.e4.
- Jun, J.J., Steinmetz, N.A., Siegle, J.H., Denman, D.J., Bauza, M., Barbarits, B., Lee, A.K., Anastassiou, C.A., Andrei, A., Aydın, Ç., et al. (2017). Fully integrated silicon probes for high-density recording of neural activity. *Nature* 551, 232–236.
- Kampa, B.M., Letzkus, J.J., and Stuart, G.J. (2006). Cortical feed-forward networks for binding different streams of sensory information. *Nat. Neurosci.* 9, 1472–1473.
- Kawaguchi, Y., and Kubota, Y. (1997). GABAergic cell subtypes and their synaptic connections in rat frontal cortex. *Cereb. Cortex* 7, 476–486.
- Kim, D., Jeong, H., Lee, J., Ghim, J.-W., Her, E.S., Lee, S.-H., and Jung, M.W. (2016a). Distinct Roles of Parvalbumin- and Somatostatin-Expressing Interneurons in Working Memory. *Neuron* 92, 902–915.
- Kim, H., Åhrlund-Richter, S., Wang, X., Deisseroth, K., and Carlén, M. (2016b). Prefrontal Parvalbumin Neurons in Control of Attention. *Cell* 164, 208–218.
- Koukoulis, F., Rooy, M., Tziotis, D., Sailor, K.A., O'Neill, H.C., Levenga, J., Witte, M., Nilges, M., Changeux, J.-P., Hoeffler, C.A., et al. (2017). Nicotine reverses hypofrontality in animal models of addiction and schizophrenia. *Nat. Med.* 23, 347–354.
- Lara, A.H., Elsayed, G.F., Zimnik, A.J., Cunningham, J.P., and Churchland, M.M. (2018). Conservation of preparatory neural events in monkey motor cortex regardless of how movement is initiated. *Elife* 7, e31826.
- Lee, S.-H., and Dan, Y. (2012). Neuromodulation of brain states. *Neuron* 76, 209–222.
- Lee, S., Kruglikov, I., Huang, Z.J., Fishell, G., and Rudy, B. (2013). A disinhibitory circuit mediates motor integration in the somatosensory cortex. *Nat. Neurosci.* 16, 1662–1670.
- Letzkus, J.J., Wolff, S.B.E., and Lüthi, A. (2015). Disinhibition, a Circuit Mechanism for Associative Learning and Memory. *Neuron* 88, 264–276.

- Li, N., Chen, T.-W., Guo, Z.V., Gerfen, C.R., and Svoboda, K. (2015). A motor cortex circuit for motor planning and movement. *Nature* 519, 51–56.
- Li, N., Daie, K., Svoboda, K., and Druckmann, S. (2016). Robust neuronal dynamics in premotor cortex during motor planning. *Nature* 532, 459–464.
- Lübke, J., and Feldmeyer, D. (2007). Excitatory signal flow and connectivity in a cortical column: focus on barrel cortex. *Brain Structure and Function* 212, 3–17.
- Maimon, G., and Assad, J.A. (2006). A cognitive signal for the proactive timing of action in macaque LIP. *Nat. Neurosci.* 9, 948–955.
- Mao, T., Kusefoglou, D., Hooks, B.M., Huber, D., Petreanu, L., and Svoboda, K. (2011). Long-range neuronal circuits underlying the interaction between sensory and motor cortex. *Neuron* 72, 111–123.
- Margrie, T.W., Brecht, M., and Sakmann, B. (2002). In vivo, low-resistance, whole-cell recordings from neurons in the anaesthetized and awake mammalian brain. *Pflügers Arch.* 444, 491–498.
- Mathis, A., Mamidanna, P., Cury, K.M., Abe, T., Murthy, V.N., Mathis, M.W., and Bethge, M. (2018). DeepLabCut: markerless pose estimation of user-defined body parts with deep learning. *Nat. Neurosci.* 21, 1281–1289.
- Mehta, M.R., Lee, A.K., and Wilson, M.A. (2002). Role of experience and oscillations in transforming a rate code into a temporal code. *Nature* 417, 741–746.
- Murakami, M., Vicente, M.I., Costa, G.M., and Mainen, Z.F. (2014). Neural antecedents of self-initiated actions in secondary motor cortex. *Nat. Neurosci.* 17, 1574–1582.
- Otsuka, T., and Kawaguchi, Y. (2008). Firing-pattern-dependent specificity of cortical excitatory feed-forward subnetworks. *J. Neurosci.* 28, 11186–11195.
- Packer, A.M., and Yuste, R. (2011). Dense, unspecific connectivity of neocortical parvalbumin-positive interneurons: a canonical microcircuit for inhibition? *J. Neurosci.* 31, 13260–13271.
- Pfeffer, C.K., Xue, M., He, M., Huang, Z.J., and Scanziani, M. (2013). Inhibition of inhibition in visual cortex: the logic of connections between molecularly distinct interneurons. *Nat. Neurosci.* 16, 1068–1076.
- Pi, H.-J., Hangya, B., Kvitsiani, D., Sanders, J.I., Huang, Z.J., and Kepecs, A. (2013). Cortical interneurons that specialize in disinhibitory control. *Nature* 503, 521–524.
- Polack, P.-O., Friedman, J., and Golshani, P. (2013). Cellular mechanisms of brain state-dependent gain modulation in visual cortex. *Nat. Neurosci.* 16, 1331–1339.
- Poulet, J.F.A., and Petersen, C.C.H. (2008). Internal brain state regulates membrane potential synchrony in barrel cortex of behaving mice. *Nature* 454, 881–885.
- Poulet, J.F.A., Fernandez, L.M.J., Crochet, S., and Petersen, C.C.H. (2012). Thalamic control of cortical states. *Nat. Neurosci.* 15, 370–372.
- Quintana, J., and Fuster, J.M. (1999). From perception to action: temporal integrative functions

of prefrontal and parietal neurons. *Cereb. Cortex* 9, 213–221.

Roitman, J.D., and Shadlen, M.N. (2002). Response of neurons in the lateral intraparietal area during a combined visual discrimination reaction time task. *J. Neurosci.* 22, 9475–9489.

Rudy, B., Fishell, G., Lee, S., and Hjerling-Leffler, J. (2011). Three groups of interneurons account for nearly 100% of neocortical GABAergic neurons. *Dev. Neurobiol.* 71, 45–61.

Scheggia, D., Managò, F., Maltese, F., Bruni, S., Nigro, M., Dautan, D., Latuske, P., Contarini, G., Gomez-Gonzalo, M., Requeie, L.M., et al. (2020). Somatostatin interneurons in the prefrontal cortex control affective state discrimination in mice. *Nat. Neurosci.* 23, 47–60.

Schiemann, J., Puggioni, P., Dacre, J., Pelko, M., Domanski, A., van Rossum, M.C.W., and Duguid, I. (2015). Cellular mechanisms underlying behavioral state-dependent bidirectional modulation of motor cortex output. *Cell Rep.* 11, 1319–1330.

Schmidt-Hieber, C., and Häusser, M. (2013). Cellular mechanisms of spatial navigation in the medial entorhinal cortex. *Nat. Neurosci.* 16, 325–331.

Schmidt-Hieber, C., and Nolan, M.F. (2017). Synaptic integrative mechanisms for spatial cognition. *Nat. Neurosci.* 20, 1483–1492.

Schneider, D.M., Nelson, A., and Mooney, R. (2014). A synaptic and circuit basis for corollary discharge in the auditory cortex. *Nature* 513, 189–194.

Stark, E., Eichler, R., Roux, L., Fujisawa, S., Rotstein, H.G., and Buzsáki, G. (2013). Inhibition-induced theta resonance in cortical circuits. *Neuron* 80, 1263–1276.

Svoboda, K., and Li, N. (2018). Neural mechanisms of movement planning: motor cortex and beyond. *Curr. Opin. Neurobiol.* 49, 33–41.

Tanaka, M. (2007). Cognitive signals in the primate motor thalamus predict saccade timing. *J. Neurosci.* 27, 12109–12118.

Thura, D., and Cisek, P. (2014). Deliberation and commitment in the premotor and primary motor cortex during dynamic decision making. *Neuron* 81, 1401–1416.

Verduzco-Flores, S., Bodner, M., Ermentrout, B., Fuster, J.M., and Zhou, Y. (2009). Working memory cells' behavior may be explained by cross-regional networks with synaptic facilitation. *PLoS One* 4, e6399.

Wagner, M.J., Kim, T.H., Kadmon, J., Nguyen, N.D., Ganguli, S., Schnitzer, M.J., and Luo, L. (2019). Shared Cortex-Cerebellum Dynamics in the Execution and Learning of a Motor Task. *Cell* 177, 669–682.e24.

Wang, Y., Toledo-Rodriguez, M., Gupta, A., Wu, C., Silberberg, G., Luo, J., and Markram, H. (2004). Anatomical, physiological and molecular properties of Martinotti cells in the somatosensory cortex of the juvenile rat. *J. Physiol.* 561, 65–90.

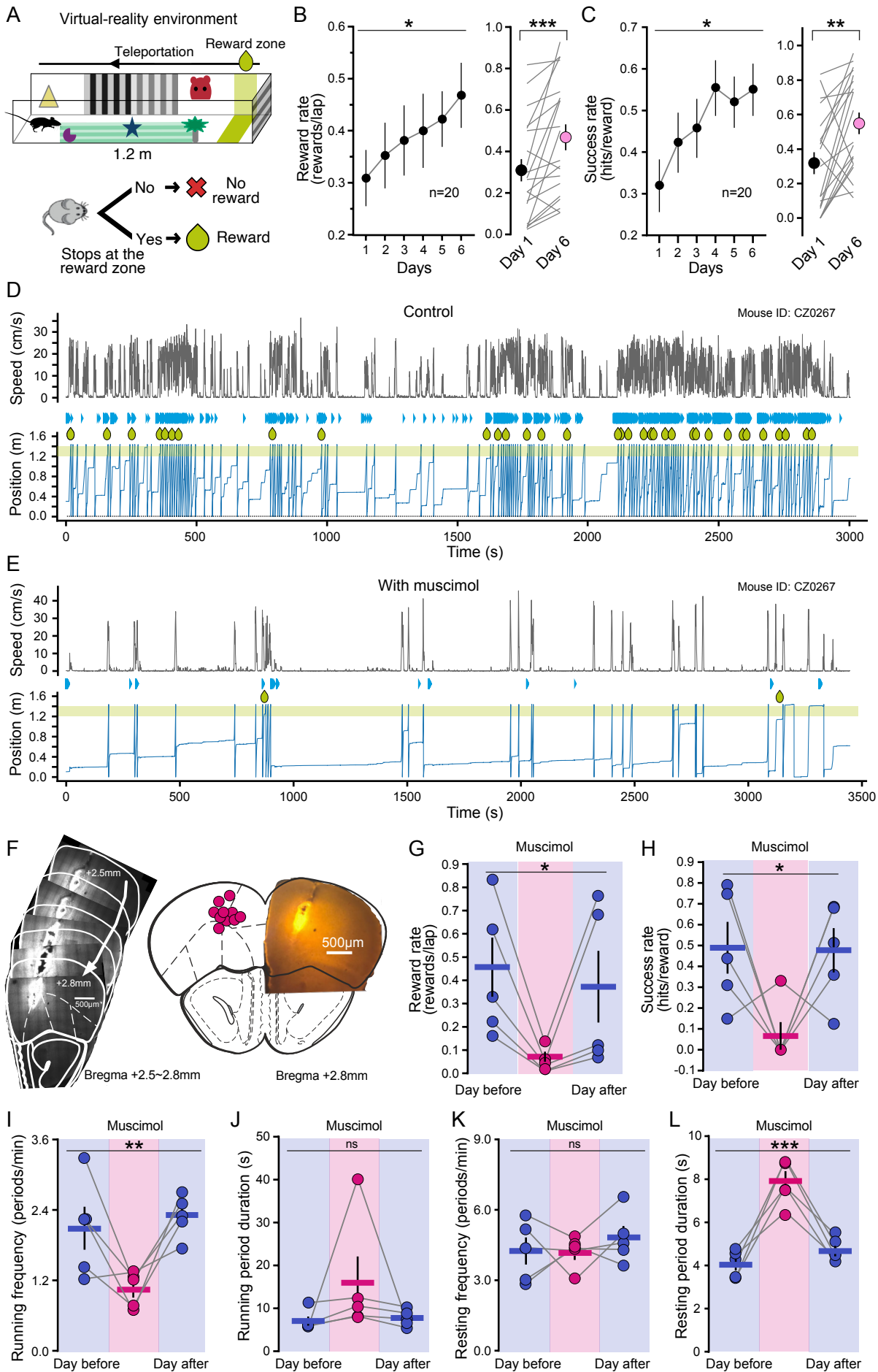
Wolff, S.B.E., Gründemann, J., Tovote, P., Krabbe, S., Jacobson, G.A., Müller, C., Herry, C., Ehrlich, I., Friedrich, R.W., Letzkus, J.J., et al. (2014). Amygdala interneuron subtypes control fear learning through disinhibition. *Nature* 509, 453–458.

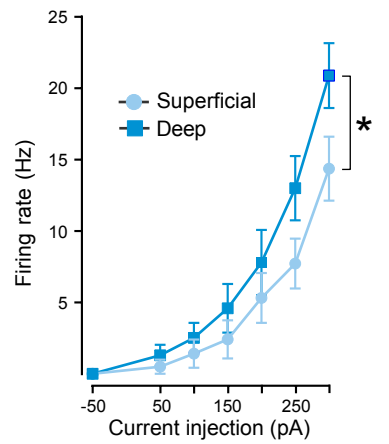
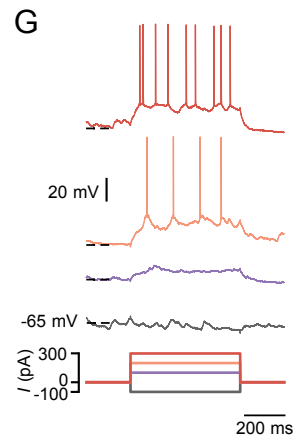
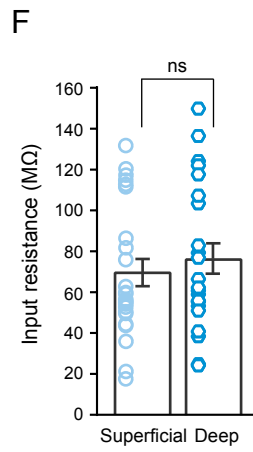
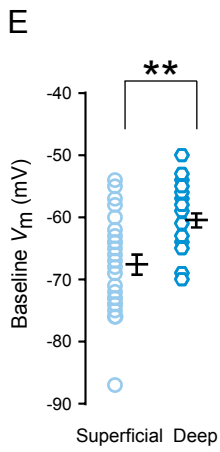
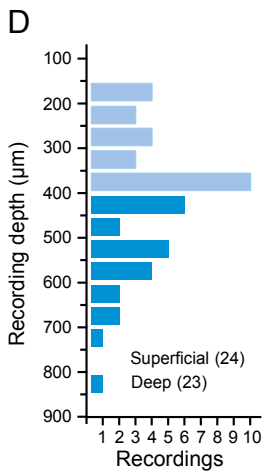
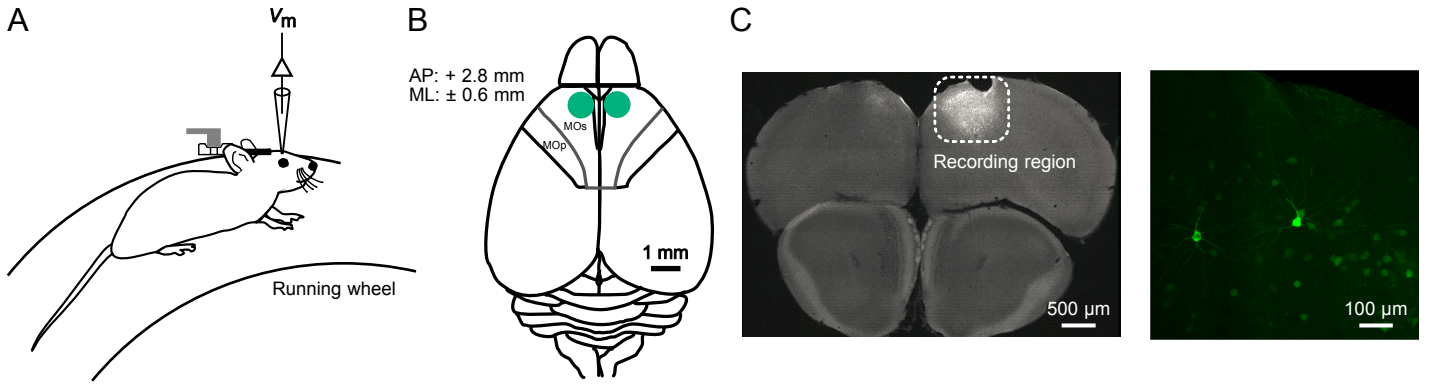
Yartsev, M.M., Hanks, T.D., Yoon, A.M., and Brody, C.D. (2018). Causal contribution and dynamical encoding in the striatum during evidence accumulation. *Elife* 7, e34929.

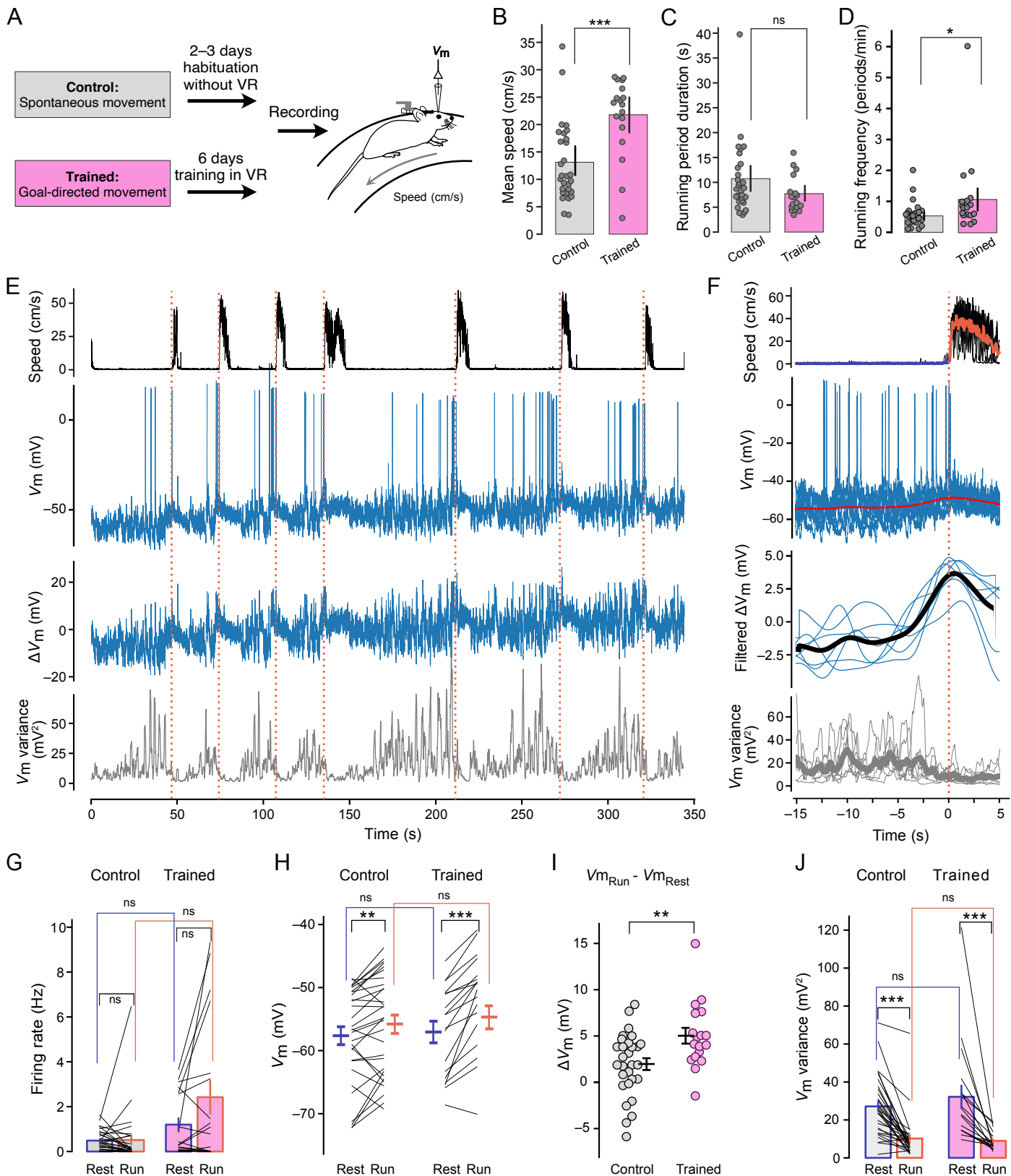
Zagha, E., Casale, A.E., Sachdev, R.N.S., McGinley, M.J., and McCormick, D.A. (2013). Motor cortex feedback influences sensory processing by modulating network state. *Neuron* 79, 567–578.

Zhao, W.-J., Kremkow, J., and Poulet, J.F.A. (2016). Translaminar Cortical Membrane Potential Synchrony in Behaving Mice. *Cell Rep.* 15, 2387–2399.

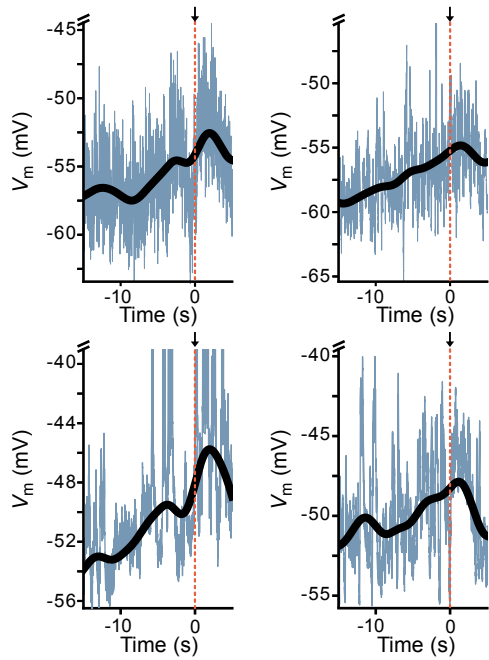
Zhou, M., Liang, F., Xiong, X.R., Li, L., Li, H., Xiao, Z., Tao, H.W., and Zhang, L.I. (2014). Scaling down of balanced excitation and inhibition by active behavioral states in auditory cortex. *Nat. Neurosci.* 17, 841–850.



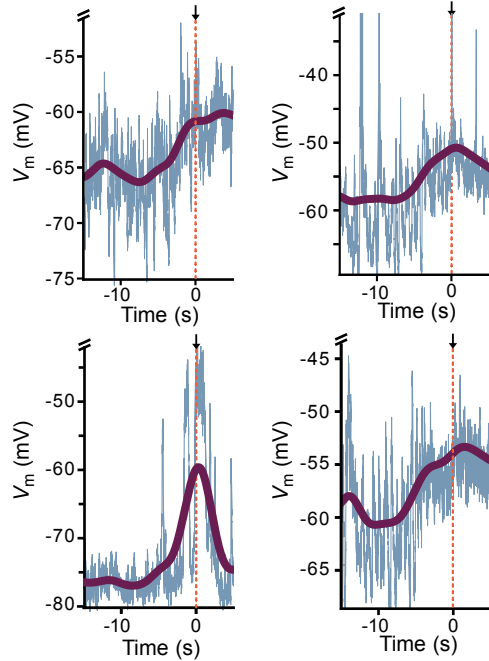




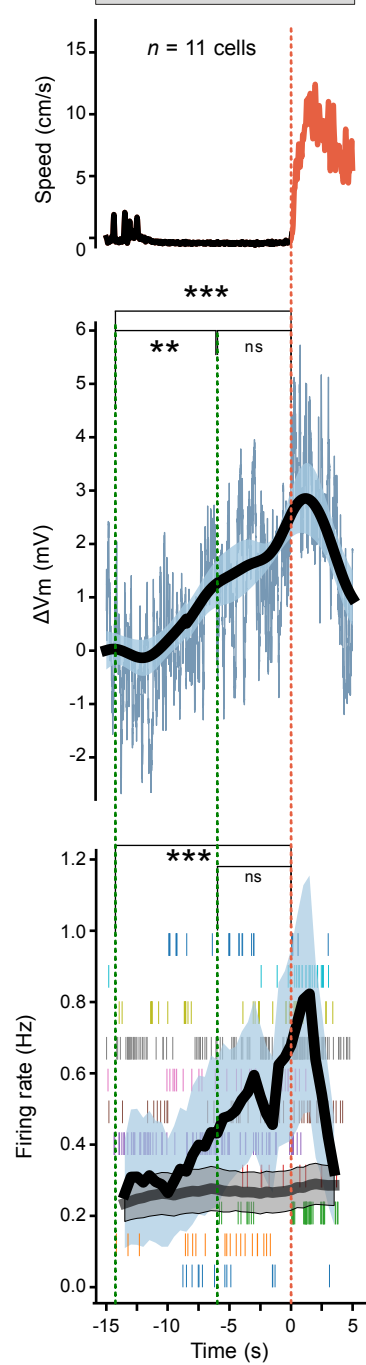
A Spontaneous movement



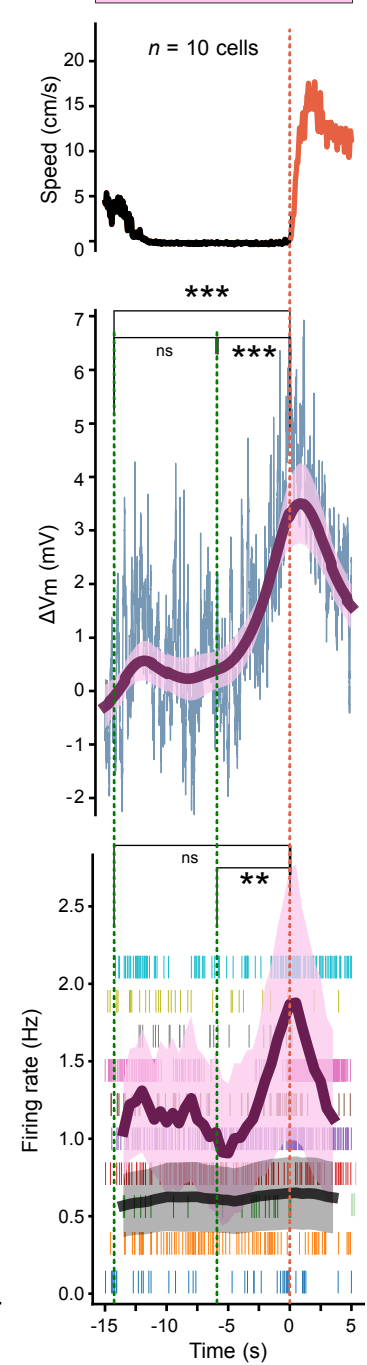
B Goal-directed movement

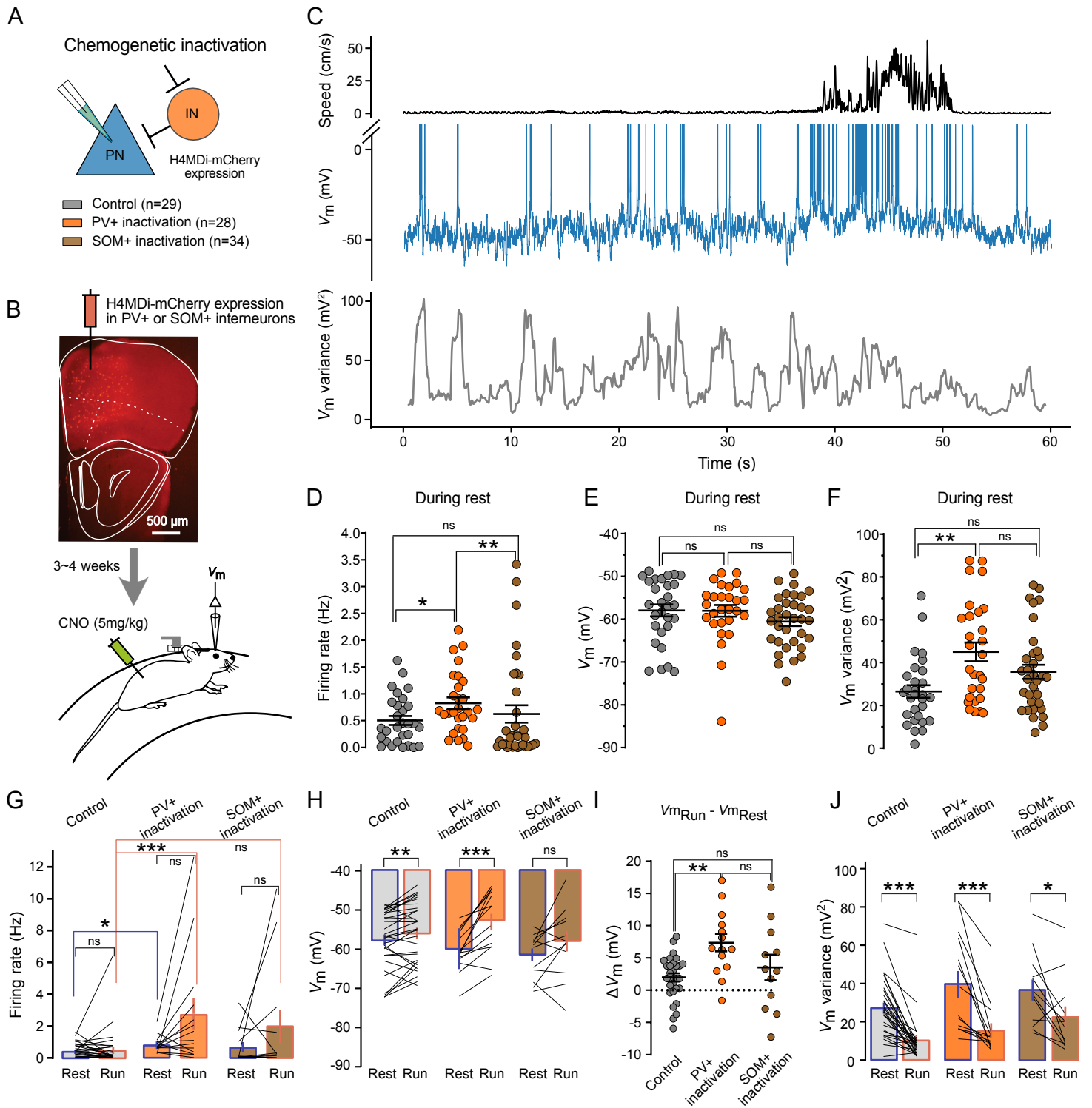


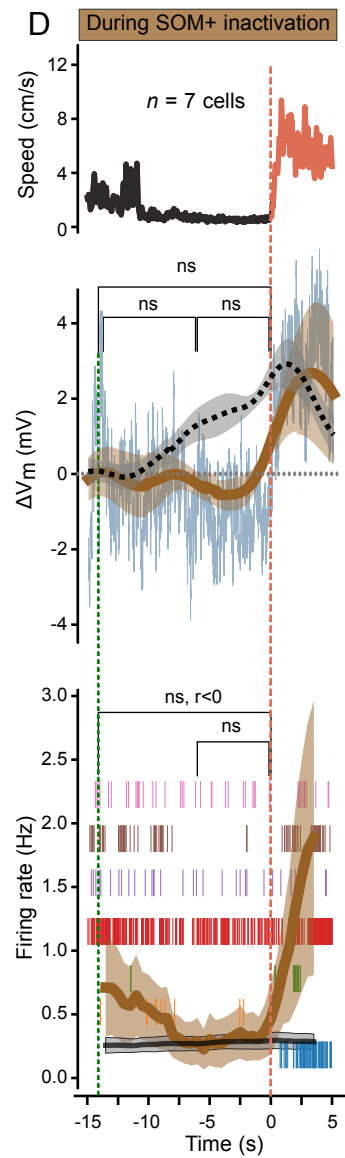
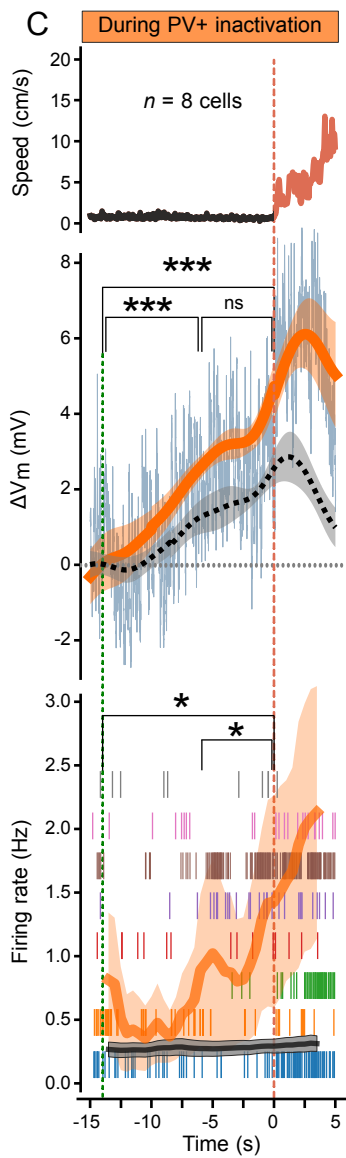
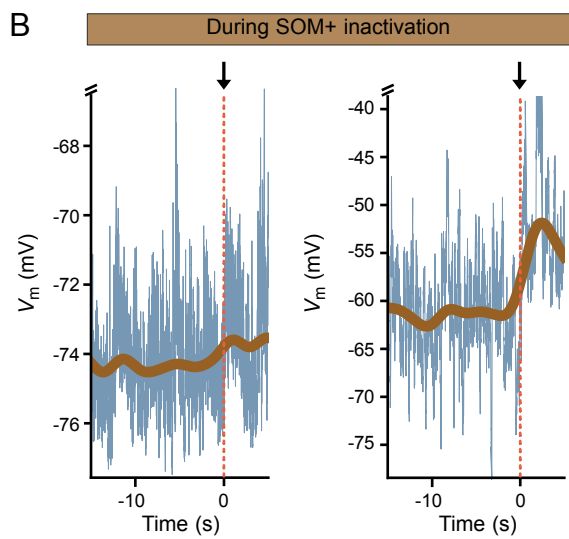
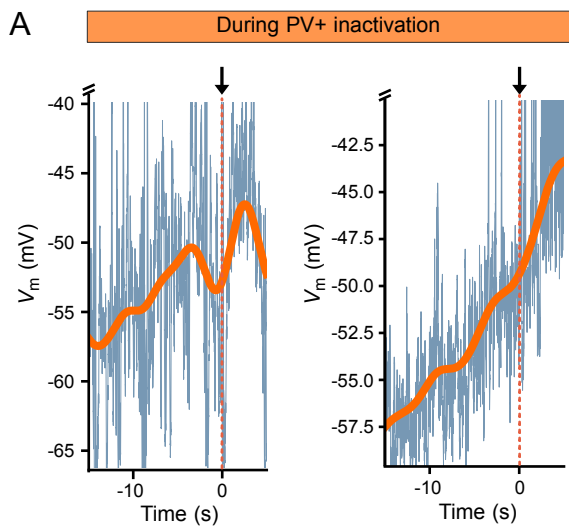
C Spontaneous movement



D Goal-directed movement







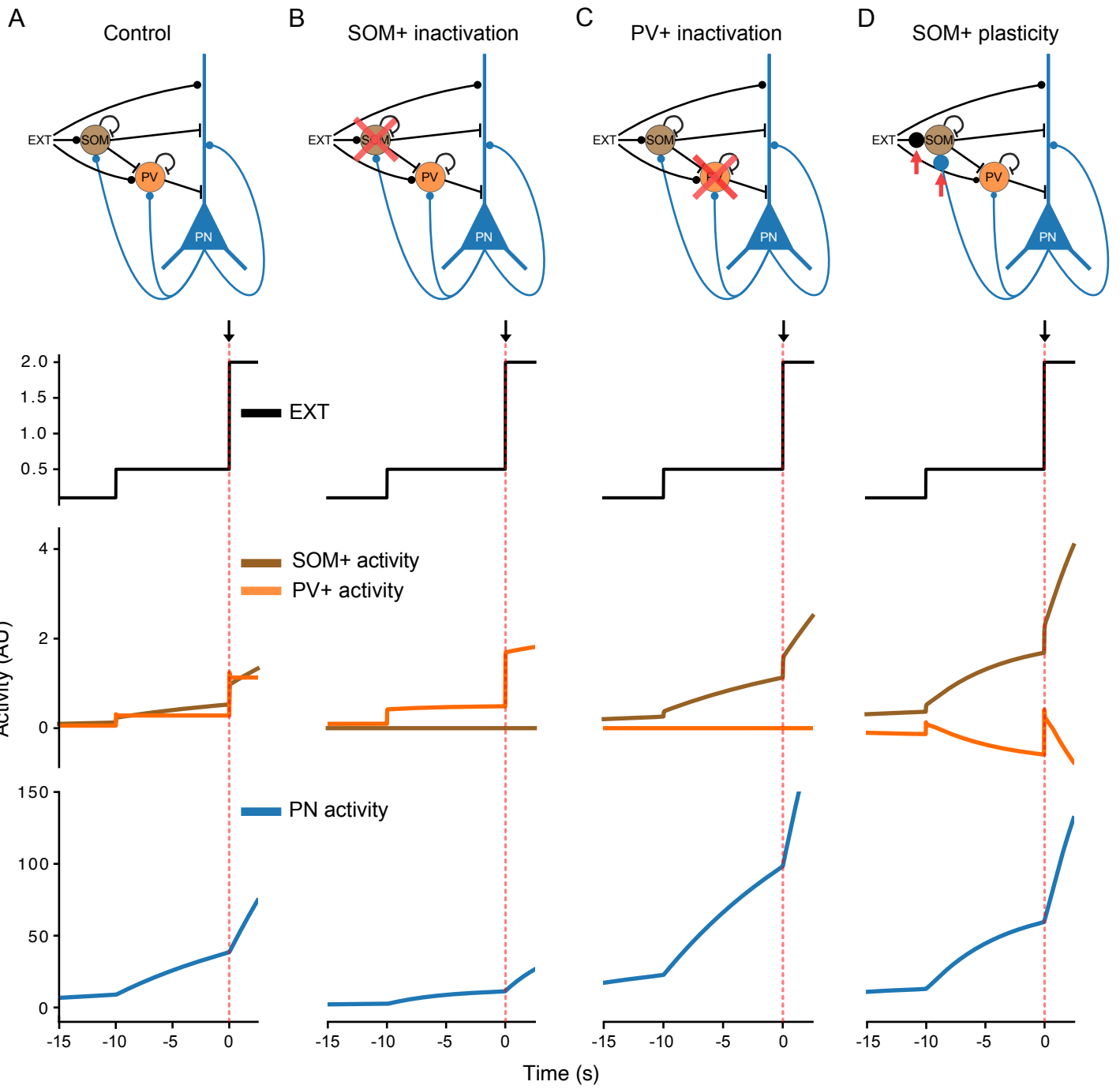


Figure S1

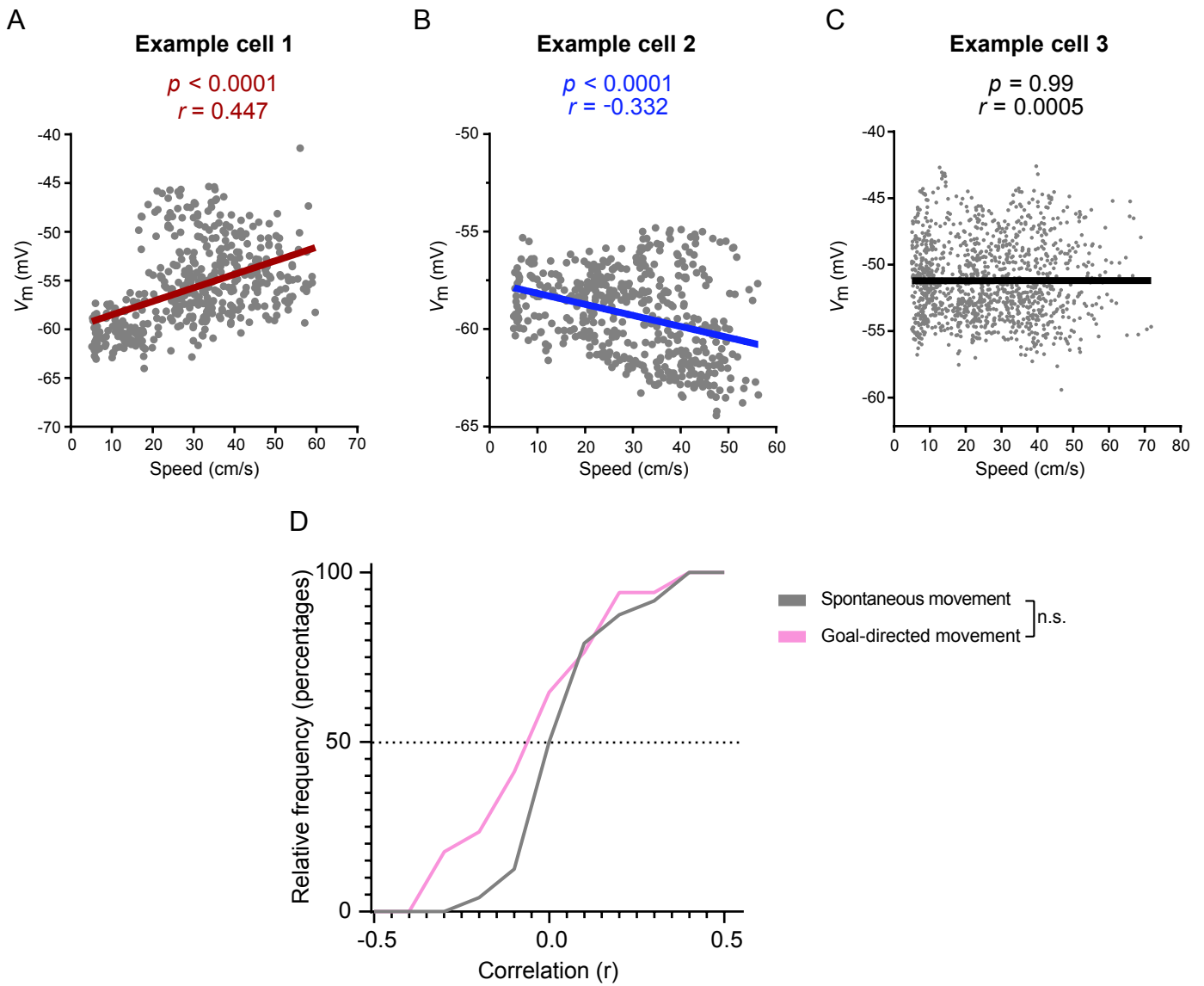


Figure S1. Heterogeneous relationship between membrane potential and animal speed. Related to Figure 3.

(A) Example recording with positive correlation between membrane potential and speed.

(B) Example recording with negative correlation between membrane potential and speed.

(C) Example recording without significant correlation between membrane potential and speed.

(D) Distribution of membrane potential – speed correlations, indicating that different types of relationships were similarly distributed across recordings. Statistical significance was assessed using a Kolmogorov-Smirnov test (D). ns, not significant.

Figure S2

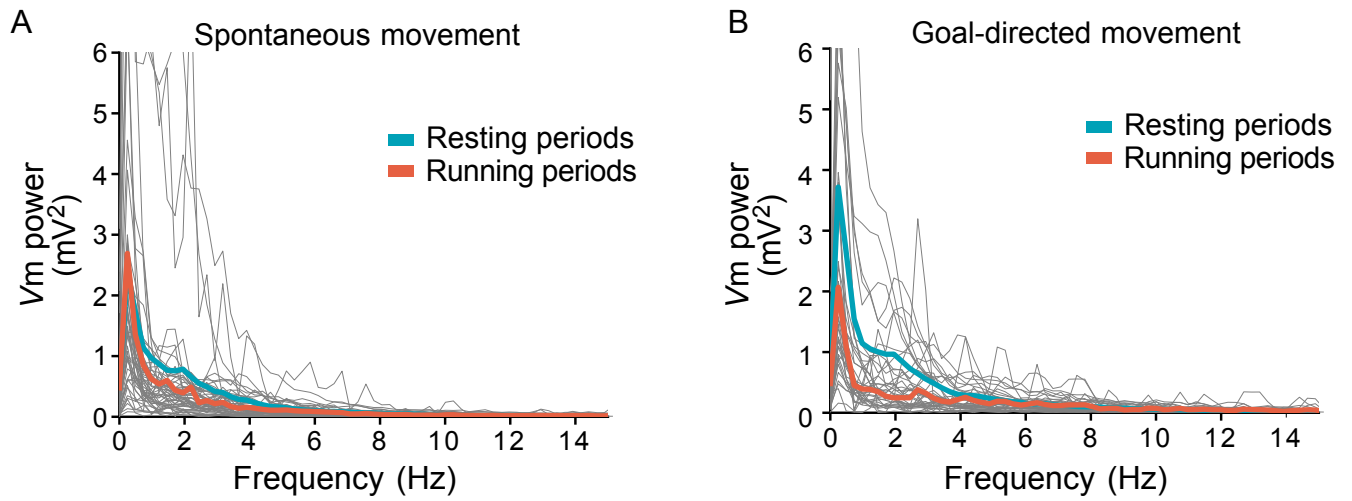


Figure S2. Membrane potential fluctuations contain broadband frequency components without any obvious peak in the spectrum. Related to Figure 3.

(A) Power spectrum density for recordings from animals running spontaneously. Grey lines represent individual recordings. Thick lines represent the means across recordings during resting periods (blue) and running periods (red).
(B) Same as in (A) for recordings from animals trained in a goal-directed task.

Figure S3

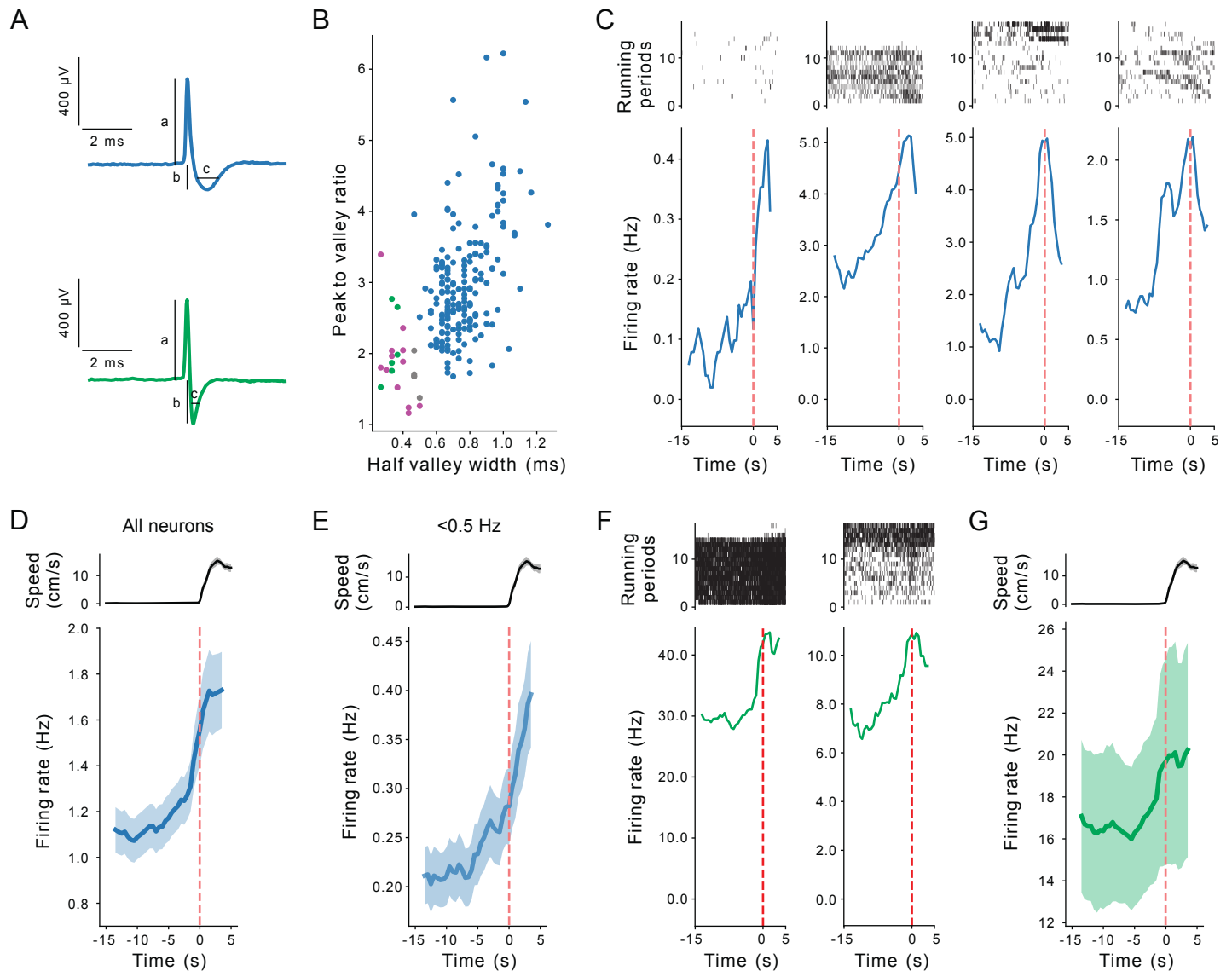


Figure S3. Extracellular recordings of population activity from MOs of spontaneously running animals. Related to Figures 3 and 4.

(A) Example spike waveforms obtained from a putative principal neuron (top) and from a putative interneuron (bottom). Traces represent mean of all action potentials produced by this unit after spike sorting. Parameters used for cell identification are indicated (a: peak; b: valley; c: half valley width).

(B) Cell type identification was performed by fitting a gaussian mixture model to the units based on the peak-to-valley ratio against half valley width. Circles correspond to individual neurons and are color-coded by putative type. Blue: principal neurons; green: fast-spiking interneurons; violet: slow-spiking interneurons; grey: low confidence assignment. Violet and grey were not used for further analysis.

(C) Example recordings from individual putative principal neurons. Data were aligned to onset of running periods at $t = 0$ s (red dashed line). Top graphs show spike rasters for the neuron over several running periods. Bottom traces show mean firing rates for the neuron across all running periods ($n = 17$ periods).

(D) Mean firing rates across all putative principal neurons ($n = 182$ neurons) aligned to onset of running periods at $t = 0$ s. Top graph shows mean speed across all running periods. Shaded regions indicate \pm s.e.m. Note slow ramp-up of spiking at $\sim t = -10$ s.

(E) Mean firing rates across low firing rates putative principal neurons (< 0.5 Hz, $n = 66$ neurons) aligned to onset of running periods at $t = 0$ s. Shaded regions indicate \pm s.e.m. Note slow ramp-up of spiking at $\sim t = -10$ s.

(F) Example recordings from individual putative fast-spiking interneurons, presented as examples in (C).

(G) Mean firing rates across all putative interneurons aligned to onset of running periods at $t = 0$ s. Note slow ramp-up of spiking at $\sim t = -5$ s.

Figure S4

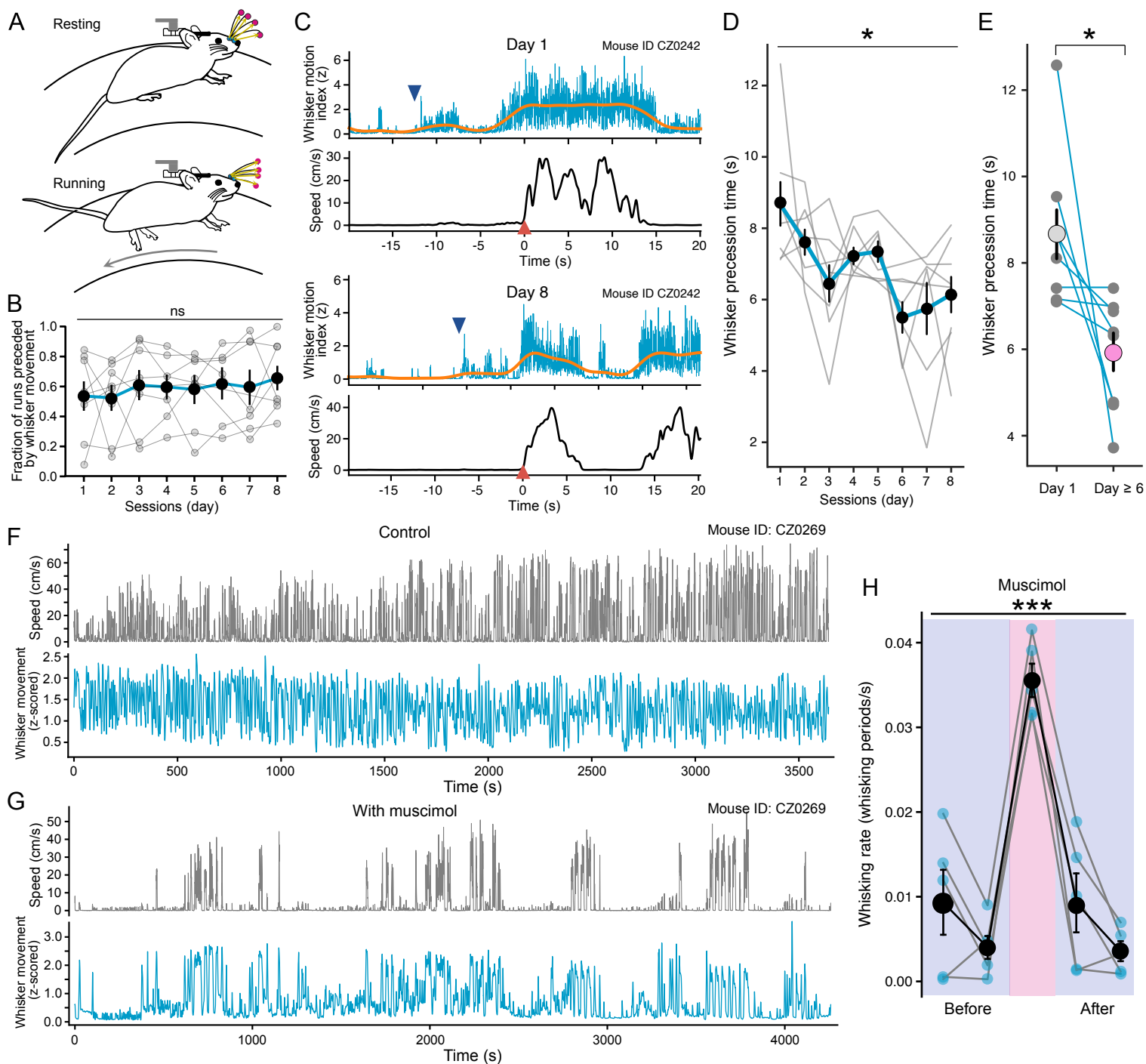


Figure S4. Whisker motion precedes running onset. Related to Figures 3 and 4.

(A) Illustration of whisker tracking during resting (top) and running states (bottom). Filled circles indicate labels (whisker bases and tips) identified by DeepLabCut.

(B) Fraction of runs preceded by whisker movement. Grey traces and grey symbols represent individual animals, blue trace and black symbols represent the mean across animals.

(C) Whisker motion index and animal speed are plotted against time during two example running periods. Blue traces represent raw data, red traces represent low-pass filtered data. The blue triangle indicates onset of whisker movement, the red triangle indicates running onset ($t = 0$ s).

(D) Whisker precession time (i.e. the difference between the times indicated by the red and blue arrows in B) is plotted against training session number. Grey traces represent individual animals, blue trace and black symbols represent the mean across animals. * indicates statistical significance.

(E) Comparison of whisker precession times between the first session (8.68 ± 0.68 s) and the mean of sessions on day 6 (5.94 ± 0.50 s) or later. Small symbols and lines represent individual animals, large symbols represent mean across animals. * indicates statistical significance.

(F-G) Example training sessions from the same mouse under control conditions (F) and after muscimol application the next day (G). Top traces show animal speed, bottom traces show z-scored whisker movement.

(H) Whisker movement period frequency (per second) of 5 mice during muscimol application, compared with two days before and after muscimol application. During muscimol application, whisking appears in discrete bouts, leading to an apparent increase in whisker movement period frequency.

Error bars represent s.e.m. Statistical significance was assessed using ordinary one-way ANOVA (B) and repeated measures ANOVA (D and H), and Wilcoxon signed rank tests (E) for day 1 vs day 6. ns, not significant; * $p < 0.05$, *** $p < 0.001$. Mean values, s.e.m., and statistics details are provided in Table S1.

Figure S5

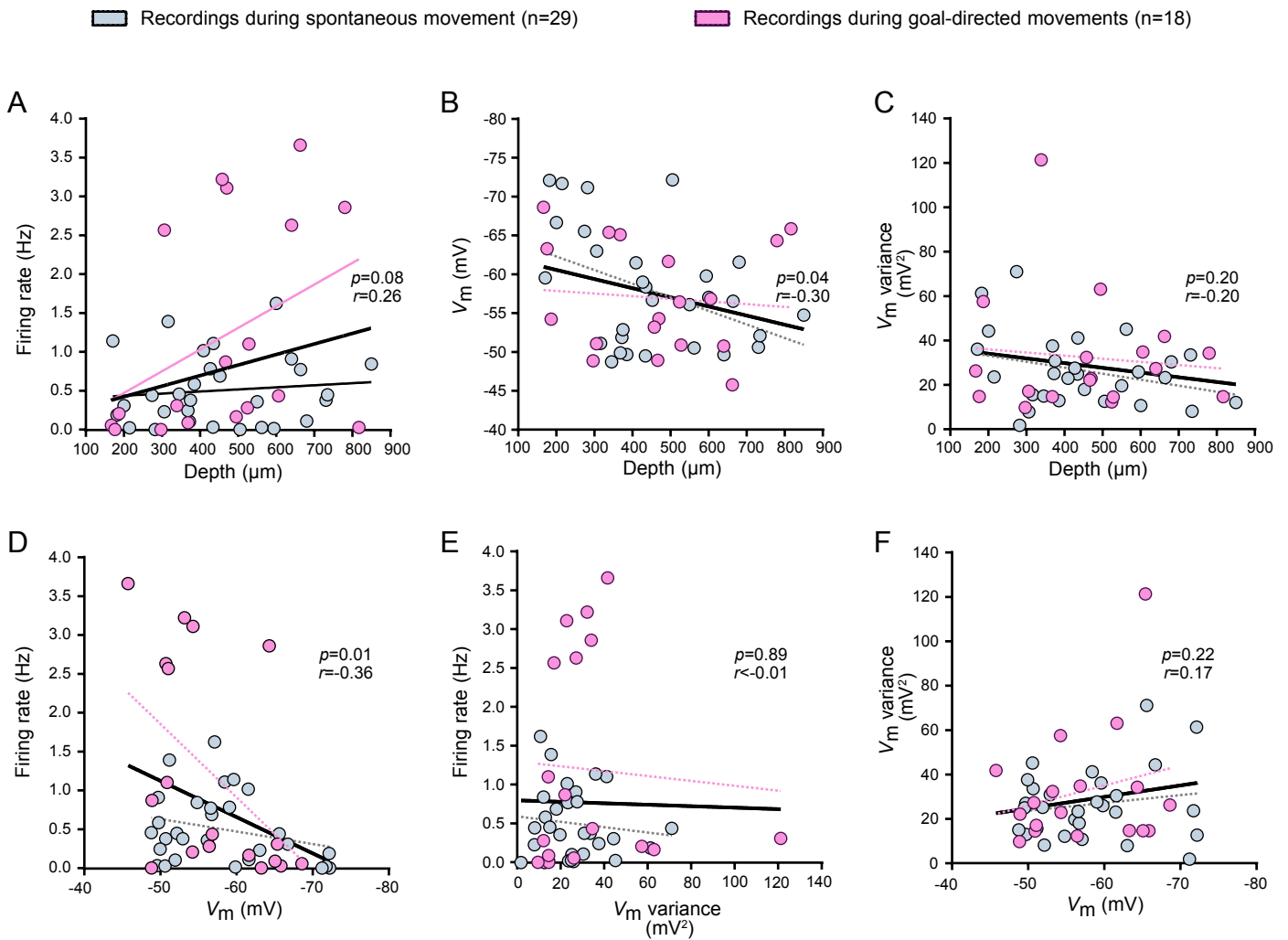


Figure S5. Relationships between firing rates, membrane potential dynamics, and recording depth. Related to Figure 3.

(A–C), Relationships between firing rate (A), baseline membrane potential (B), membrane potential variance (C) and recording depth for untrained (grey) and trained (pink) animals.

(D–F), Relationships between firing rate and membrane potential (D), firing rate and membrane potential variance (E), and membrane potential variance and membrane potential (F) for untrained (grey) and trained (pink) animals.

Statistics values and black lines refer to linear regression analysis applied to all recordings from trained and untrained animals.

Figure S6

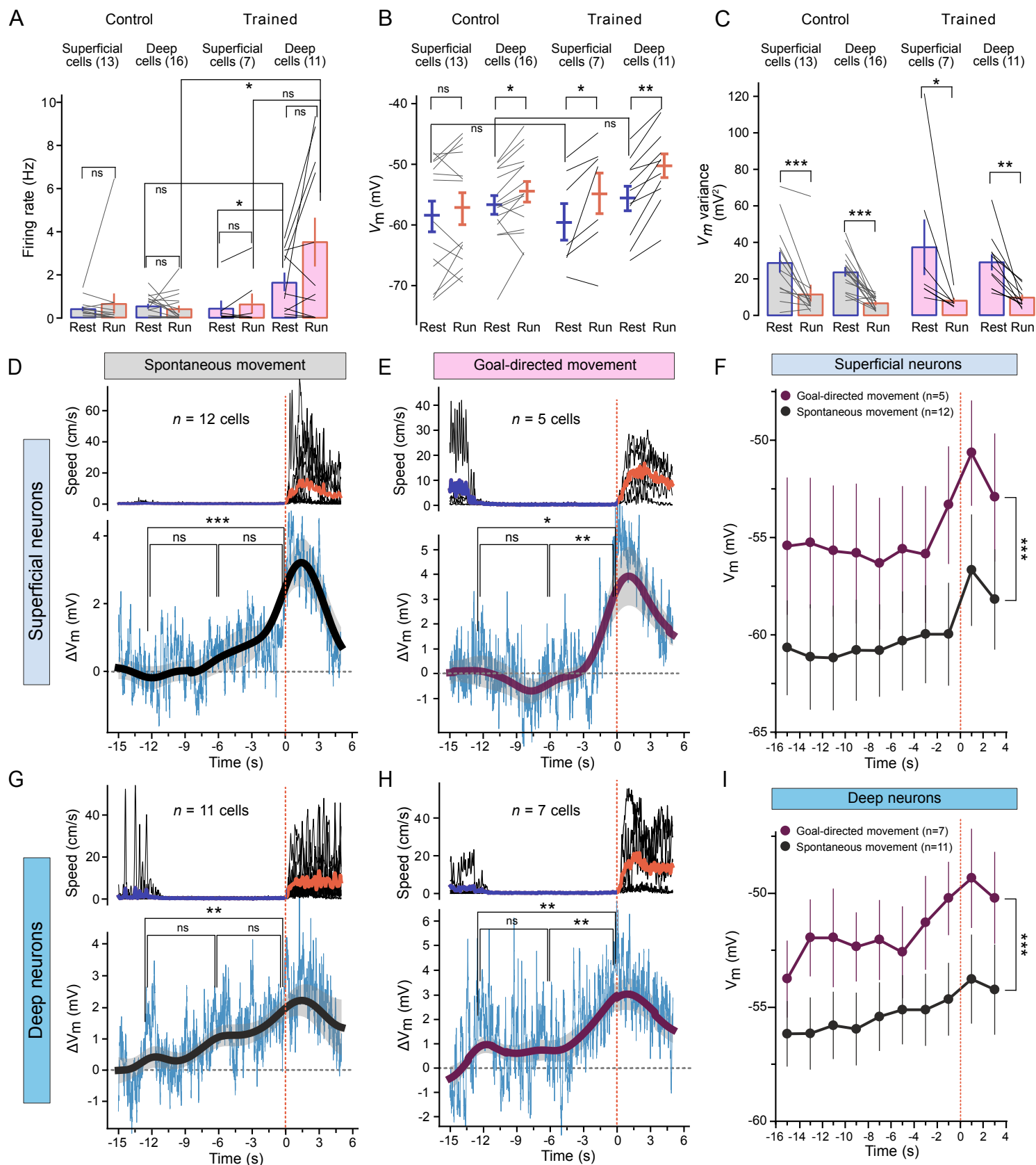


Figure S6. Subthreshold membrane potential ramps precede the onset of movement in both superficial and deep neurons. Related to Figures 3 and 4.

(A-C) Summary of firing rates (A; superficial neurons in control group: resting 0.42 ± 0.12 Hz vs running 0.67 ± 0.51 Hz, $n = 13$; deep neurons in control group: resting 0.57 ± 0.12 Hz vs running 0.44 ± 0.17 Hz, $n = 16$; superficial neurons in trained group: resting 0.48 ± 0.38 Hz vs running 0.67 ± 0.50 Hz, $n = 7$; deep neurons in trained group: resting 1.67 ± 0.45 Hz vs running 3.53 ± 1.18 Hz, $n = 11$) mean V_m (B; superficial control resting -59.6 ± 2.7 mV vs running -58.0 ± 2.7 mV; deep control resting -56.7 ± 1.5 mV vs running -54.4 ± 1.7 mV; superficial trained resting -59.5 ± 3.2 mV vs running -54.8 ± 3.7 mV; deep trained resting -55.4 ± 2.0 mV vs running -50.1 ± 2.0 mV) and V_m variance (C; superficial control resting 29.5 ± 5.9 mV² vs running 12.2 ± 4.8 mV²; deep control resting 24.0 ± 2.7 mV² vs running 7.2 ± 0.9 mV²; superficial trained resting 37.2 ± 16.5 mV² vs running 7.9 ± 1.7 mV²; deep trained resting 29.0 ± 4.7 mV² vs running 9.6 ± 1.7 mV²) during resting (blue) and running periods (red) for all recordings from the control and trained groups in superficial and deep neurons (control superficial cells at 291 ± 22 μ m; control deep cells at 579 ± 34 μ m; trained superficial cells at 263 ± 34 μ m; trained deep cells at 586 ± 40 μ m).

(D-E) Summary of membrane potential changes (ΔV_m) aligned to the onset of running periods in superficial neurons ($n = 12$ recordings from control animals (D), $n = 5$ recordings from trained animals (E)). Data were aligned to the onset of running periods as shown in Fig. 4C–D. Mean V_m between $t = -15$ s and $t = -10$ s was used as a baseline to calculate ΔV_m . Top, mean animal speed. Bottom, mean membrane potential (thin traces), mean low-pass filtered membrane potential (thick traces, shaded regions represent mean \pm s.e.m). Note that all spiking and non-spiking neurons which have enough long recording periods before and after onset of movements are included in the figure (see Methods).

(F) Comparison of mean V_m in superficial neurons between the control group and the trained group during resting and running periods. Data were binned in 2-s time bins ($F = 7.846$, $p = 0.0004$).

(G-H) Same as in (D–E) for recordings from deep neurons ($n = 11$ recordings from control animals (G), and $n = 7$ recordings from trained animals (H)).

(I) Same as (F) for recordings from deep neurons ($F = 11.02$, $p < 0.0001$ for I).

For this figure, the data set shown in Figure 3 was split into recordings from deep and superficial neurons.

Error bars represent \pm s.e.m. Statistical significance was assessed by Wilcoxon signed rank tests (A–C) for paired groups, and Mann-Whitney tests (A–B) for unpaired groups, Spearman's correlation (D–E and G–H) and two-way ANOVA with Bonferroni post-hoc tests (F and I). ns, not significant; * $p < 0.05$; ** $p < 0.01$; *** $p < 0.001$. Mean values, s.e.m., and statistics details are provided in Table S1.

Figure S7

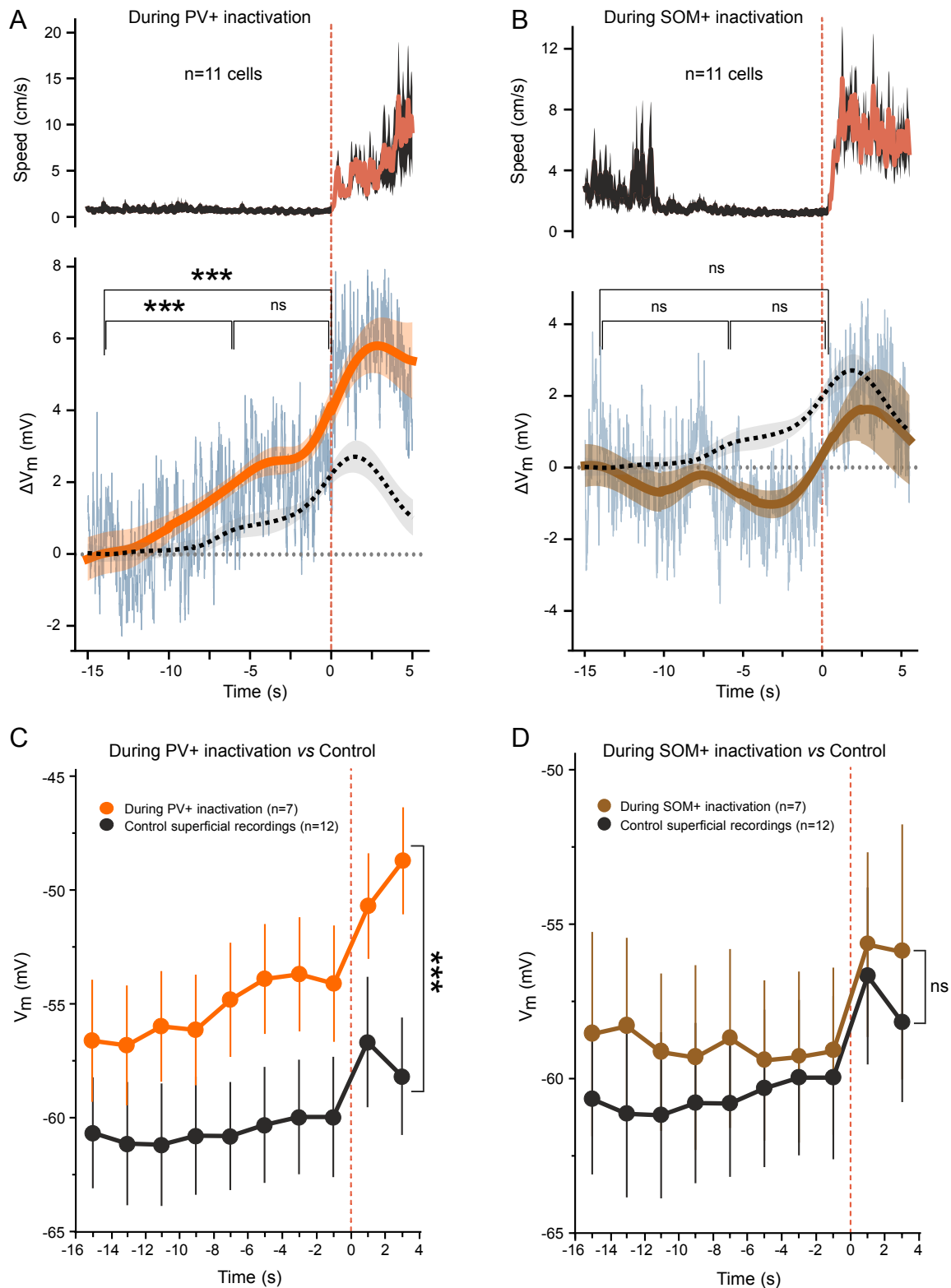


Figure S7. Inactivation of local PV+ in MOs, leads to depolarized membrane potential before and during running onset. Related to Figures 5 and 6.

(A-B) Summary of speed and membrane potential of all spiking and non-spiking recordings preceding movement onset during chemogenetic inactivation of PV+ interneurons (A, $n = 11$; 8 spiking and 3 non-spiking neurons) or of SOM+ interneurons (B, $n = 11$; 7 spiking and 4 non-spiking neurons). Recordings from only the spiking subset of these recordings is shown in Figure 6C-D. Data are aligned to running onset at $t = 0$ s (indicated by a red vertical dashed line). Top, mean animal speed. Bottom, mean membrane potential (thin traces), mean low-pass filtered membrane potential (thick traces, shaded regions represent mean \pm s.e.m). The black dash traces represent the control recordings including spiking and non-spiking neurons ($n = 23$; 11 spiking and 12 non-spiking neurons).

(C-D) Comparison of mean V_m in superficial neurons between control recordings (black, same as shown in Figure S6F) and recordings during PV+ inactivation (orange) aligned to the onset of running periods. Data were binned in 2-s time bins ($F = 11.10$, $p < 0.0001$). Same as (C) for recordings from superficial neurons during inactivation of SOM+ interneurons ($F = 0.7720$, $p = 0.2454$).

Error bars represent \pm s.e.m. Statistical significance was assessed by Spearman's correlation (A-B) and two-way ANOVA with Bonferroni post-hoc tests (C-D). ns, not significant; * $p < 0.05$; ** $p < 0.01$; *** $p < 0.001$. Statistics details are provided in Table S1.

Table S2. Synaptic weights in the reduced model of the local PFC circuit. Related to Figure 7.

<i>Presynaptic</i>	<i>Postsynaptic</i>	<i>Weight (AU)</i>
External inputs	Principal neuron	1.0
	PV+ interneuron	1.0
	SOM+ interneuron	0.3
Principal neuron	Principal neuron	1.0
	PV+ interneuron	0.01
	SOM+ interneuron	0.01
PV+ interneuron	Principal neuron	-1.0
	PV+ interneuron	-0.25
	SOM+ interneuron	-0.01
SOM+ interneuron	Principal neuron	-0.25
	PV+ interneuron	-1.0
	SOM+ interneuron	0